Thermodynamic and mechanical properties of lanthanum–magnesium phases from density functional theory

J. Wróbel [a,*], L.G. Hector Jr. [b], W. Wolf [c], S.L. Shang [d], Z.K. Liu [d], K.J. Kurzydłowski [a]

[a] Faculty of Materials Science and Engineering, Warsaw University of Technology, ul. Wołoska 141, 02-507 Warszawa, Poland
[b] GM R&D Center, 30500 Mound Road, Warren, MI 48090-9055, USA
[c] Materials Design s.a.r.l., 44 avenue F.-A. Bartholdi, 72000 Le Mans, France
[d] Department of Materials Science and Engineering, The Pennsylvania State University, Steidle Building, University Park, PA 16802, USA

ARTICLE INFO

ABSTRACT

Thermodynamic and mechanical properties of the six known phases in the La–Mg phase diagram, viz. LaMg, $LaMg_2$, $LaMg_3$, La_5Mg_{41}, La_2Mg_{17}, and $LaMg_{12}$, and their elemental antecedents, Mg and La, are computed with density functional theory (DFT) using the PBE and PBEsol exchange-correlation functionals. Phase stability analyses show that both $LaMg_2$ and La_5Mg_{41} are metastable at low temperatures which is consistent with experiments and vibrational spectra. We generalize an existing approach for computing the crystallographic dependence of Young's modulus and Poisson's ratio, which is presently limited to cubic systems, to address any space group symmetry using 0 K elasticity tensor components (C_{ij}) from DFT. Isothermal and isentropic $C_{ij}(T)$ are computed with the quasiharmonic approximation (QHA) as are the linear thermal expansion of the cubic compounds, the average linear thermal expansion for the non-cubic compounds, the bulk modulus, and the constant pressure heat capacity. A critical comparison of theoretical results from the PBE and PBEsol functionals is made with available experimental data.

© 2011 Elsevier B.V. All rights reserved.

1. Introduction

Six known La–Mg compounds with cubic, hexagonal, tetragonal, and orthorhombic space group symmetries form through combination of Mg and La, two hexagonal metals. The La–Mg compounds, viz., LaMg, $LaMg_2$, $LaMg_3$, La_5Mg_{41}, La_2Mg_{17}, $LaMg_{12}$, display a rich variety of thermodynamic and mechanical properties. For example, some of the La–Mg compounds have been identified as strengthening phases in Mg alloys [1], while others are potential hydrogen storage materials and hydride anodes for Ni/MH (MH = metal hydride) batteries. Of particular interest are their oxidation resistance, high temperature ductility, and low temperature superconductivity [2,3]. Some of the La–Mg compounds have a catalytic effect on hydrogen absorption and desorption in various materials [4–13]. Other applications include components of switchable or tunable mirrors [14]. Lanthanum has been used as an additive to various Mg alloys (currently of interest to transportation industries as light weight replacement materials) in studies of creep resistance, strength enhancement, casting porosity, and corrosion resistance [15–21]. Gaps in our knowledge of thermodynamic and mechanical (e.g. elastic) properties of the La–Mg

compounds remain despite significant prior experimental effort. Much of this effort is a consequence of their intriguing properties.

Considerable attention has been directed toward generating an accurate La–Mg phase diagram with experimental methods [22–25]. Guo and Du [24] provided a history of La–Mg phase diagram development which appears to have begun with the work of Canneri [25] in 1931. Nayeb-Hashemi and Clark [23] described five compounds (LaMg, $LaMg_2$, $LaMg_3$, La_2Mg_{17} and $LaMg_{12}$) in the La–Mg phase diagram. A refinement to the phase diagram was subsequently published by Okamoto [26]. A sixth compound, La_5Mg_{41}, was reported by Giovannini et al. [27], but this does not (as of yet) appear in any La–Mg phase diagram. Of these six compounds, it is only $LaMg_{12}$ for which a definitive (fully occupied) structure remains in question. A more recent assessment of the La–Mg phase diagram may be found in Berche et al. [28].

First-principles density functional theory (DFT) has been used to explore a small number of properties of various La- and Mg-containing compounds in Refs. [2,29–34]. Future alloy designs from computational thermodynamics via the CALPHAD approach [35] will likely rely upon DFT-predicted properties in the absence of experimental data [36–39]: careful validation of these properties against relevant experimental data is critical. At the present time, a comprehensive DFT investigation of thermodynamic and mechanical properties of the six known La-Mg compounds is unavailable. Vibrational and fundamental thermodynamic property data, such as the temperature dependence of the linear

* Corresponding author.
  E-mail addresses: jan.wrobel@inmat.pw.edu.pl, jwrobel00@gmail.com
(J. Wróbel).

thermal expansion, $\alpha_L(T)$, and the constant pressure heat capacity, $C_p(T)$, is sparse, and there are only two DFT studies of the mechanical properties of these materials that could be located in the extant literature [33,40].

In this article, we present a comprehensive first-principles DFT investigation of thermodynamic and mechanical properties of the six known La–Mg compounds along with their elemental antecedents Mg and La. The goal of our study was two-fold: to provide properties of the La–Mg compounds that cannot readily be located in the literature, and to demonstrate the versatility of DFT for material property predictions. We compute lattice constants, enthalpies of formation and phase stability, and the 0 K (single crystal) elasticity tensor components, C_{ij}, using DFT within the Perdew–Burke–Ernzerhof (PBE) and PBEsol (PBE solid) exchange-correlation functionals. Elastic anisotropy is investigated (PBE only) with computed Young's modulus and Poisson's ratio surfaces which are color contours showing crystallographic dependence of these important mechanical properties. We compare results for the computed linear thermal expansion, $\alpha_L(T)$, for the cubic La–Mg compounds, the average linear thermal expansion, $\alpha_L^*(T)$, for the non-cubic La–Mg compounds, the isothermal bulk modulus, $B(T)$, and the constant pressure heat capacity, $C_p(T)$, from the PBE and the PBEsol functionals. Anharmonicity due to thermal expansion is addressed with the quasiharmonic approximation (QHA). The QHA within the PBE is also used to compute both the $C_{ij}^T(T)$ (isothermal elasticity tensor components) and $C_{ij}^S(T)$ (isentropic elasticity tensor components) for each compound. Several fully occupied LaMg$_{12}$ structures have been proposed in the literature. We show that the electronic energies of two of these LaMg$_{12}$ structures, viz., a fully occupied LaMg$_{12}$ Immm orthorhombic structure with a giant unit cell, and that with the ThMn$_{12}$-type I4/mmm structure are very close. We note that thermal expansion and heat capacity are critical inputs to models of a wide variety of physical phenomena. Examples include material models of strain-induced phase transitions in high strength steels (e.g. transformation induced plasticity) that liberate heat, and models of battery and hydrogen storage propulsion systems [41–47]. These quantities are often assumed to be constants, or values used in models are best guesses since experimental measurements from room temperature to melting are often difficult or non-existent. The paucity of experimental data for the La–Mg phases provided motivation for computing properties with both the PBE and PBEsol functionals.

2. Structures and known properties

The La–Mg compounds are metals, and bonding has been attributed to electrons in the Mg 3s and 2p and La 5d and 4f shells [32]. Cohesive energies decrease with increasing Mg concentration [32]. Stability ranges of the La–Mg compounds were discussed in De Negri et al. [48] and Berche et al. [28].

LaMg crystallizes in the Pm-3m space group (#221) and has the cP2-CsCl-type structure with $a = 3.97$ Å [49] (reported lattice constants are assumed to be room temperature values). Buschow [50] observed that LaMg (with a Mg mole fraction of $x_{Mg} = 0.5$) is a Pauli paramagnet. Morishita et al. [51] identified a superconducting phase transition at 5.9 K from measurements of $C_p(T)$: this is approximately 1 K above that in elemental La. LaMg$_2$ ($x_{Mg} = 0.667$) has the cF24-MgCu$_2$ structure with the Fd-3m space group (#227) and $a = 8.806$ Å [52]. Single crystal data was reported by Belgacem et al. [53]. Raghavan [54] discussed the stability of LaMg$_2$ at 673 K. Nayeb-Hashemi and Clark [23] suggested that LaMg$_2$ forms by a peritectic reaction (liquid + LaMg$_3$ ↔ LaMg$_2$) at 998 K and decomposes by a eutectoid reaction (LaMg$_2$ ↔ LaMg + LaMg$_3$) at 1048 K. LaMg$_3$ ($x_{Mg} = 0.75$) has the cF16-BiF$_3$ structure with space group Fm-3m (#225) and lattice constant $a = 7.51$ Å [52]. It has

been shown to absorb hydrogen to 4 wt.% at 300 °C [6]. Buschow found that LaMg$_3$ is a Pauli paramagnet [55] and Yamamoto et al. [56] observed that the LaMg$_3$ valence band consists primarily of free electron gas-like Mg electrons with strongly localized 4f electrons from La. LaMg$_3$ has a narrow composition range at high temperatures [57]. The La$_5$Mg$_{41}$ structure ($x_{Mg} = 0.891$), which was first reported by Giovannini et al. [27], is isostructural with tI92-Ce$_5$Mg$_{41}$ [58] and has the tetragonal space group I4/m (#87, $a = b = 14.822$ Å, $c = 10.468$ Å). According to De Negri et al. [48], La$_5$Mg$_{41}$ decomposes eutectoidaly below 873 K. The La$_2$Mg$_{17}$ ($x_{Mg} = 0.895$) phase is hexagonal (P63/mmc, $a = b = 10.36$ Å, $c = 10.24$ Å) with the hP38-Th$_2$Ni$_{17}$ structure [59] and its composition is very close to that of La$_5$Mg$_{41}$. It has been investigated as a potential hydride electrode material [13,60], hydrogen storage material [12,61,62], and was recently identified as a precipitate in Mg–Zn–Y–La alloys [1]. Within 543–563 K, LaMg$_{12}$ and La$_2$Mg$_{17}$ under hydrogen decompose to LaH$_3$ and MgH$_2$ [63]. As the most Mg-rich compound in the La–Mg phase diagram ($x_{Mg} = 0.923$), LaMg$_{12}$ has attracted substantial interest as a potential hydrogen storage material. A fully occupied structure for LaMg$_{12}$, however, remains a topic of ongoing research with two LaMg$_{12}$ polymorphs thought to be similar to experimentally-confirmed structures of CeMg$_{12}$. These are: an anti-phase, body-centered orthorhombic structure, oI338-Immm (#71), which is isotructural with Immm CeMg$_{12}$, first reported by Johnson et al. [64]; and a tetragonal tI26-I4/mmm (#139) structure based upon ThMn$_{12}$ with lattice parameters $a = b = 10.33$ Å, $c = 5.96$ Å (note that experimental data are reported for CeMg$_{12}$) [65]. In a study of hydrogen storage in LaMg$_{12}$, Pal [66] identified a tetragonal structure with lattice parameters $a = 10.34 \pm 0.05$ Å and $c = 71.53 \pm 0.05$ Å but no additional structural information was provided. It is interesting to note that the Immm structure of CeMg$_{12}$ proposed by Johnson et al. [64] could not be confirmed by Deportes et al. [67]. However, Sun et al. [63,68] found that a LaMg$_{12}$ Immm structure with lattice constants $a = 10.34420 \pm 0003$ Å, $b = 10.36520 \pm 0015$ Å, and $c = 77.58620 \pm 0014$ Å was the best fit to their XRD data. They observed that LaMg$_{12}$ has a composition range rather than a well-defined stoichiometry, and nuclear coordinates of a fully occupied Immm cell were therefore not provided. Interaction with hydrogen induces phase decomposition of LaMg$_{12}$ to La$_2$Mg$_{17}$, which has greater thermodynamic stability. Denys et al. [69] identified an orthorhombic (Immm) LaMg$_{10.85}$ with lattice parameters $a = 10.3391(5)$ Å, $b = 10.3554(5)$ Å, $c = 77.484(4)$ Å. This non-stoichiometric structure is similar to that for CeMg$_{12}$ reported by Johnson et al. [64] where the cell is constructed with 13-ThMn$_{12}$-type tetragonal units stacked along [0 0 1]. Units are "slipped" by $0.5a$ at $z = 0.1345$; $1/2 - z$; $1/2 + z$ and $1 - z$) along planes (or "nets") of Mg sites. This cell structure was also suggested by Giovanni et al. [27]. Interestingly, the hydrogen storage capacity of LaMg$_{12}$ alloy has been reported to reach 3.7–5.5 wt.% [66]. Using rapid solidification for grain size refinement in hydrogen storage, Poletaev et al. [70] recently identified a new La–Mg phase, viz., an hexagonal TbCu$_7$ structure, along with the previously reported ThMn$_{12}$ and LaMg$_{11}$ (orthorhombic) phases. Relevant structural details for all materials investigated in this study are summarized in Table 1.

3. Computational methodology

All calculations in this study are conducted with the Vienna Ab Initio Simulation Package (VASP), a plane wave DFT code [71–73]. The electron–ion interactions are described by the full potential projector augmented wave (PAW) method [74]. Exchange-correlation is treated within the generalized gradient approximation GGA-PBE [75]. To explore predictions from another

Table 1
Space group symmetries and VASP computational parameters for electronic energies and phonons. 500 eV plane wave cut-off energy used for all calculations. Atomic displacements in phonon calculations: ± 0.02 Å. x_{Mg} = mole fraction of Mg. S.U. = symmetry-unique.

Material (x_{Mg})	Pearson symbol	Space group (No.)	Structure type	Electronic $\bar{k}$-mesh (#S.U. $\bar{k}$-points)	Phonon Supercell (# atoms)	Phonon $\bar{k}$-mesh (#S.U. $\bar{k}$-points)
Mg	hP2	P63/mmc (194)	–	$25 \times 25 \times 25$ (845)	$4 \times 4 \times 2$ (64)	$6 \times 6 \times 4$ (15)
La	hP4	P63/mmc (194)	–	$21 \times 21 \times 7$ (192)	$3 \times 3 \times 1$ (36)	$5 \times 5 \times 5$ (15)
LaMg (0.5)	cP2	Pm-3m (221)	CsCl	$25 \times 25 \times 25$ (455)	$3 \times 3 \times 3$ (54)	$5 \times 5 \times 5$ (10)
LaMg$_2$ (0.67)	cF24	Fd-3m (227)	MgCu$_2$	$25 \times 25 \times 25$ (455)	$2 \times 2 \times 2$ (192)	$5 \times 5 \times 5$ (4)
LaMg$_3$ (0.75)	cF16	Fm-3m (225)	BiF$_3$	$25 \times 25 \times 25$ (455)	$2 \times 2 \times 2$ (128)	$5 \times 5 \times 5$ (4)
La$_5$Mg$_{41}$ (0.891)	tI92	I4/m (87)	Ce$_5$Mg$_{41}$	$9 \times 9 \times 9$ (105)	$1 \times 1 \times 1$ (92)	$3 \times 3 \times 5$ (9)
La$_2$Mg$_{17}$ (0.895)	hP38	P63/mmc (194)	Th$_2$Ni$_{17}$	$13 \times 13 \times 13$ (147)	$1 \times 1 \times 1$ (38)	$4 \times 4 \times 4$ (12)
LaMg$_{12}$ (0.92)	tI26	I4/mmm (139)	ThMn$_{12}$	$17 \times 17 \times 17$ (405)	$1 \times 1 \times 2$ (52)	$5 \times 5 \times 5$ (18)

exchange-correlation functional, selected properties are also computed in the GGA-PBEsol [76]. The strengths and weaknesses of different local and semi-local functionals for various materials and their properties have been assessed in several studies. For example, lattice parameters and bulk moduli for selected metals, semiconductors and insulators as obtained from LDA, PBE, and PBEsol and other functionals were compared to experimental data in [77–80]. Consistently, LDA tends to strongly underestimate and PBE tends to overestimate lattice parameters, respectively. Alternatively, LDA tends to overestimate, while PBE underestimates, respectively, binding energies, elastic properties (e.g. bulk moduli), surface energies, and phonon frequencies. Although for some materials LDA or PBE still exhibit best agreement with experiment, PBEsol tends to improve the overall agreement to these experimental data on bulk properties due to reduced dependence of the enhancement factors on the gradient [76]. The PBEsol is, however, less accurate than LDA for atomic properties as reflected in computed atomization energies (for example).

The core configurations for the La and Mg PAW potentials are [Kr]4d^{10} and [He]2s^2, respectively. Structural parameters for the thermodynamic and mechanical property calculations are optimized by simultaneously minimizing all atomic forces and stress tensor components via a conjugate gradient method. Three successive full-cell optimizations are conducted to ensure convergence of cell energies and structural parameters. Total energies are calculated using the fully relaxed structures by integration over a Monkhorst-Pack mesh of k-points in the Brillouin zone with the linear tetrahedron method with Blöchl corrections. The plane wave cutoff energy for all calculations is 500 eV. In all cases, the total energy is converged to 10^{-7} eV/cell and the force components are relaxed to at least 10^{-4} eV/Å.

Phonon spectra for the solids and associated thermodynamic functions are computed by means of the supercell (direct) approach to lattice dynamics with VASP as the computational engine [81]. The cell size in each phonon calculation is chosen such that computed force constants at its boundaries are negligible. For some La–Mg compounds, the conventional cell is found to meet these criteria, whereas supercells are required for the others. Additional details on the supercell method may be found in [82,83]. The cells used in the phonon calculations along with VASP $\bar{k}$-point meshes are detailed in Table 1.

4. Quasiharmonic approximation of thermodynamics

Central to the QHA is minimization of the Helmholtz free energy, $F(V,T)$, with respect to variations of all internal degrees of freedom at several fixed cell volumes [84]. In practice, the QHA has been found to work best for many solids up to some temperature between the Debye temperature and the melting point [30,85–88]. Within the QHA, $F(V,T)$ is usually expressed as,

$$F(V, T) = E(V) + F_{elec}(V, T) + F_{phonon}(V, T) \tag{1}$$

where $E(V)$ is the 0 K static energy excluding any thermal contributions, with the first-principles predicted $E(V)$ data points fit by the Birch–Murnaghan (B–M) equation-of-state (EOS) [89], $F_{elec}(V,T)$ the thermal electronic free energy, and $F_{phonon}(V,T)$ the vibrational Helmholtz free energy (for additional details see [86,88,90]). Remaining thermodynamic properties, such as, entropy S, enthalpy H, isothermal bulk modulus $B(T)$, volume thermal expansion α_V, constant volume (or isochoric) heat capacity C_V, and constant pressure heat capacity,

$$C_p(T) = C_V(T) + \alpha_V^2(V, T)TB(T)V_0(T) \tag{2}$$

are obtained from the QHA-determined $F(V,T)$. Here, $C_v(T)$ is the constant volume heat capacity (from phonon calculations), T is temperature, and $V_0(T)$ is the equilibrium volume at temperature T.

5. Anisotropic properties: Thermal expansion and elasticity

5.1. Thermal expansion

For single crystals, some properties such as thermal expansion and the elasticity tensor components, C_{ij}, are anisotropic. Since the second-order strain tensor, ε_{ij}, is symmetric, it can be expressed in terms of six independent components ε_i,

$$\varepsilon = \begin{pmatrix} \varepsilon_{11} & \varepsilon_{12} & \varepsilon_{13} \\ \varepsilon_{21} & \varepsilon_{22} & \varepsilon_{23} \\ \varepsilon_{31} & \varepsilon_{32} & \varepsilon_{33} \end{pmatrix} = \begin{pmatrix} \varepsilon_1 & \varepsilon_6/2 & \varepsilon_5/2 \\ \varepsilon_6/2 & \varepsilon_2 & \varepsilon_4/2 \\ \varepsilon_5/2 & \varepsilon_4/2 & \varepsilon_3 \end{pmatrix} \tag{3}$$

Here, the reduced representation in terms of the ε_i is represented in matrix form [91]. With increasing temperature, six

independent linear thermal expansion components, α_{ij} (or α_i in reduced form), can be derived from the corresponding ε_{ij} (or ε_i),

$$\alpha_{ij}(T) = \left(\frac{\partial \varepsilon_{ij}(T)}{\partial T} \right)\Bigg|_P \tag{4}$$

Crystal symmetry affords a reduction in the number of independent coefficients of $\alpha_{ij}(T)$. The $\varepsilon_{ij}(T)$ are written in terms of the lattice constants, $a_i(T)$, obtained from the QHA. The values of $a_i(T)$ are first calculated at several cell volumes. These results are interpolated (via cubic spline interpolation) to obtain values of a_i for each $V_0(T)$ at selected temperatures from 0 K up to the melting point. For the hexagonal and tetragonal compounds, we computed the average thermal expansion, α_L^*, to facilitate comparison with experimental data. This is given by,

$$\alpha_L^* = \frac{\alpha_L^{\parallel} + 2\alpha_L^{\perp}}{3} = \frac{\alpha_V}{3} \tag{5}$$

where the two independent components of $\alpha_{ij}(T)$ are $\alpha_L^{\parallel}$ (along the principal axis, i.e. the c-direction, or α_{33}) and $\alpha_L^{\perp}$ (normal to the principal axis or α_{11} for hexagonal and tetragonal symmetries. For the cubic structures, we write the single linear thermal expansion component as α_L.

5.2. Elasticity tensor components C_{ij} at 0 K

Aside from their significance as fundamental (intrinsic) mechanical properties of solids, the components of the elasticity tensor, C_{ij} (arrived at by exploiting the symmetry of the fourth-order tensor C_{ijkl}) have been linked to important thermodynamic properties. For example, Fine et al. [92] found that the melting temperature of certain cubic intermetallic compounds correlates with the value of C_{11}. A correlation was also found between the C_{ij} and melting temperature of hexagonal and tetragonal compounds. A quantitative relationship between the Young's modulus (a poly-crystalline estimate of which can be derived from the C_{ij}) and the thermodynamics of hydrogen-absorption in Mg films was recently demonstrated in [93]. The values of C_{ij} are also important in studies of material defects, such as dislocations [94]. Components of the 0 K elasticity tensor, C_{ij}, are computed using the stress-based least-squares fitting method of Le Page and Saxe [95,96]. This method uses the stresses computed in the VASP code as inputs to a least-squares fit of the unknowns appearing in the linear stress–strain relationships for a selected sequence of symmetry-unique strains. For the La–Mg compounds addressed herein, the unknowns are the three, five, six and nine independent C_{ij} for cubic, hexagonal, tetragonal, and orthorhombic symmetries, respectively. The moduli are computed from the first derivatives of the stresses, rather than from the second derivatives of the total energy, with respect to strain. This method avoids the numerical difficulties often encountered with evaluations of the latter and reduces the number of VASP calculations, and all C_{ij} are computed simultaneously rather than as independent sums of C_{ij}. The calculated values of C_{ij} are sensitive to the $\vec{k}$-point mesh, and this required a series of ancillary calculations to test $\vec{k}$-point convergence of all C_{ij}. It was determined that the application of four successive strains, viz., 0.4%, 0.5% 0.6%, and 0.7% was adequate to obtain ≤1% statistical error in each computed C_{ij}. The quality of the least squares fit, as gauged by the computed least squares residual, is ≤1% for all C_{ij} calculations. The small residuals are consistent with negligible anharmonic effects in the computed C_{ij} due to the applied strains. We also compute polycrystalline bulk, shear, and Young's moduli based upon the Hill criterion [97].

5.3. Elasticity tensor components at high temperatures $C_{ij}(T)$

To calculate the isothermal elasticity tensor components, $C_{ij}^T(T)$, we first compute the 0 K C_{ij} at selected volumes above and below the equilibrium volume, $V_0(T)$, from the QHA. Using $V_0(T)$, the $C_{ij}^T(T)$ are computed via interpolation from the $C_{ij}(V)$ wherein the volume dependence is eliminated. Here, the kinetic energy and the fluctuations of microscopic stress tensors [98] are ignored. The measured elasticity tensor components at high temperatures (e.g. using the resonance method) are usually isentropic since the system is adiabatic due to the faster speed of elastic waves relative to heat diffusion [99,100]. The isentropic elasticity tensor is defined as $C_{ij}^S(T)$. From Davies [101] the $C_{ij}^S(T)$ can be written in terms of the $C_{ij}^T(T)$ as

$$C_{ij}^S(T) = C_{ij}^T(T) + \frac{TV\lambda_i\lambda_j}{C_V} \tag{6}$$

where

$$\lambda_i = -\sum_{j=1}^{6} \left(\frac{\partial \sigma_i}{\partial \varepsilon_j} \right)_T \left(\frac{\partial \varepsilon_j}{\partial T} \right)_\sigma = -\sum_{j=1}^{6} \alpha_j C_{ij}^T(T) \tag{7}$$

The reduced forms of stress, strain, and thermal expansion, denoted by σ_i, ε_j, and α_j follow the definition in Eq. (3).

5.4. Elastic anisotropy

Elastic properties of anisotropic crystalline materials often include single values of the Young's modulus or Poisson's ratio. Both properties, however, are dependent upon the direction of measurement within a crystal lattice. On a practical note, elastic anisotropy has been related to cracking near grain boundaries (in the form of microcracks and delamination) in polycrystalline materials [102,103]. A useful approach to examining elastic anisotropy is with mathematically-derived surfaces that change their shape from one crystallographic direction to the next. The extent to which the surfaces change shape is indicative of anisotropy. An existing approach for computing Young's modulus and Poisson's ratio surfaces was presented by Zhang et al. [104,105]. Their technique, however, is limited to cubic systems. In the present study, we extend the Zhang et al. [104,105] methodology to compute elastic anisotropy of hexagonal and tetragonal space group symmetries. For the La–Mg phases of interest here, we compute contours of the Young's modulus and Poisson's ratio as a function of orientation with respect to the crystal lattice. This requires calculation of the fourth-order elastic compliance tensor, S_{ijkl}, which is determined via inversion of the 0 K second-order elasticity tensor [104,105], C_{ij}.

Following Zhang et al. [104,105], the Young's modulus, $E(h\,k\,l)$, and average Poisson ratio, $\upsilon(h\,k\,l)$, along a direction normal to the lattice plane system described with Miller indices $(h\,k\,l)$ are given as

$$E(hkl) = \frac{1}{s'_{3333}} \tag{8}$$

$$\upsilon(hkl) = -\frac{s'_{1133} + s'_{2233}}{2s'_{3333}} \tag{9}$$

Here, s'_{ijkl} are components of the compliance tensor in the new reference system (the new lattice plane system rotated from the original one and described with Miller indices $(h\,k\,l)$) written in fourth-order tensor notation and transformed from the compliances of the crystal, s_{mnop}, in the original cubic crystal axes. Hence

$$s'_{ijkl} = a_{im}a_{jn}a_{ko}a_{lp}s_{mnop} \tag{10}$$

where a_{im}, a_{jn}, a_{ko}, and a_{lp} are the transformation matrices [91]. The transformation matrix, a_{rt}, from the original cubic crystal axes to the new lattice plane system described with Miller indices $(h\,k\,l)$ can be expressed explicitly in terms of Miller indices of this plane [104,105].

$$
(a_{rt}) = \begin{bmatrix} \dfrac{hl}{\sqrt{h^2+k^2}\sqrt{h^2+k^2+l^2}} & \dfrac{kl}{\sqrt{h^2+k^2}\sqrt{h^2+k^2+l^2}} & -\dfrac{\sqrt{h^2+k^2}}{\sqrt{h^2+k^2+l^2}} \\ -\dfrac{k}{\sqrt{h^2+k^2}} & \dfrac{h}{\sqrt{h^2+k^2}} & 0 \\ \dfrac{h}{\sqrt{h^2+k^2+l^2}} & \dfrac{k}{\sqrt{h^2+k^2+l^2}} & \dfrac{l}{\sqrt{h^2+k^2+l^2}} \end{bmatrix}
$$
(11)

where h, k, l are the direction cosines.

In Zhang et al. [104,105], expressions for $E(h\,k\,l)$ and $\upsilon(h\,k\,l)$ are reduced for cubic structures to a simple function of direction cosines. In the method presented here, the transformation matrix, a_{rt}, is calculated for each orientation (chosen from a uniformly distributed set of directions) and $E(h\,k\,l)$ and $\upsilon(h\,k\,l)$ are obtained from Eqs. (8)–(11). The original compliance tensor s_{mnop} is not limited to cubic space group symmetry.

6. Results and discussion

6.1. LaMg$_{12}$ structures

The fully occupied Immm LaMg$_{12}$ structure is constructed following the recipe of Johnson et al. for CeMg$_{12}$ [64]. This consists of 13-tetragonal ThMn$_{12}$-type cells [69] with a slip of 0.5a occurring at $z = 4/26$, 10/26, 17/26, and 23/26 (see supplementary materials). We have compared the computed X-ray powder patterns for the Immm structure with the experimental powder patterns in Pal [66] and Sun [68] and found reasonable agreement. For comparison with the ThMn$_{12}$ and Immm LaMg$_{12}$ structures, a smaller Pmmn (#59) LaMg$_{12}$ cell, which has not been identified in the literature, is constructed from the Immm cell with shifts of 0.5a at $z = 4/26$, 10/26 (see supplementary materials). The VASP total energies of the Immm and Pmmn structures are 0.006 and 0.001 eV/f.u. lower (i.e. more negative), respectively, than that of the ThMn$_{12}$-type I4/mmm structure, which is energetically very close. While vibrational corrections could modify this observation, phonon calculations on the Immm structure are impractical due to the large number of independent atoms in the unit cell. Hence, we use the LaMg$_{12}$ I4/mmm structure for all subsequent calculations.

6.2. Lattice constants and vibrational spectra

Calculated lattice constants from the QHA at 0 K and 298 K, along with experimental (room temperature) values, are listed in Table 2 (hcp Mg, dhcp α-La) and Table 3 (La–Mg compounds). In general, 298 K lattice constants from the PBEsol are smaller than those from the PBE, as expected. For Mg the 298K PBEsol results, and for La the 298 K PBE results, tend to be in closer accord with experimental values (see Table 2). The fact that PBE does not overestimate lattice parameters for Lanthanum (as one would expect from general trends) may be attributed to an overestimation of the contribution of f-electrons to the bonding by density functional approaches. Consistent with these results for the pure elements, PBEsol is in increasingly better agreement with experiment as Mg content increases for the 298 K lattice parameters of the La–Mg compounds. For LaMg, however, the PBE functional is still superior. The lattice parameters of all other compounds are better described by PBEsol,

Table 2
Lattice constants a, c (in Å) of Mg and La from the PBE and PBEsol. Numbers in parentheses are the VASP-optimized lattice constants based upon electronic energies only, while numbers not in parentheses were computed with the QHA. Experimental results are assumed at 298 K.

		Mg		La	
			PBE		
Å		0 K	298 K	0 K	298 K
a,b		3.21	3.23	3.77	3.78
		(3.19)		(3.76)	
c		5.19	5.23	12.08	12.11
		(5.17)		(12.06)	
			PBEsol		
Å		0 K	298 K	0 K	298 K
a,b		3.19	3.21	3.65	3.66
		(3.16)		(3.65)	
c		5.17	5.20	11.71	11.73
		(5.14)		(11.69)	
			Exp.		
a		3.2089[a]		3.772[b]	
c		5.2101[a]		12.144[b]	

[a] Ref. [106].
[b] Ref. [107].

with the c lattice parameter of La$_2$Mg$_{17}$ being the only exception (note that experimental data are not available for LaMg$_{12}$).

Computed vibrational spectra for the fully VASP-optimized (PBE) LaMg, LaMg$_2$, LaMg$_3$, La$_2$Mg$_{17}$, La$_5$Mg$_{41}$, and LaMg$_{12}$ structures are shown in the supplementary material. No imaginary phonon modes are noted.

6.3. Thermal expansion

Fig. 1a and b compare the computed α_L^* from Eq. (5) for Mg and La with experimental data [109,110]. Agreement between experiment and the PBEsol result for Mg in Fig. 1a is superior over the entire temperature range considered compared to the PBE. From Fig. 1b, a similar conclusion cannot be reached for La due to the dhcp α/fcc β phase transition at 533 K [111]. This is denoted in the experimental data by the jump at ~600 K, beyond which can be seen a substantial disagreement with the PBE and the PBEsol results. A more formal theoretical treatment of the La phase transition is required in order to accurately predict thermal expansion beyond ~600 K.

Fig. 2 compares α_L for the cubic La–Mg compounds computed with the PBE and the PBEsol. As temperature increases, we note that $(\alpha_L)_{PBE} > (\alpha_L)_{PBEsol}$. From the PBE, we find $\alpha_L^{LaMg_2} > \alpha_L^{LaMg_3} > \alpha_L^{LaMg}$. A similar trend does not result from the PBEsol since the α_L for LaMg$_2$ and LaMg$_3$ are nearly equivalent below ~410 K: beyond this point, $\alpha_L^{LaMg_2} > \alpha_L^{LaMg_3}$. Fig. 3 compares the α_L^* from the PBE and PBEsol for the three non-cubic La–Mg compounds. From the PBE, we find $(\alpha_L^*)^{LaMg_{12}} > (\alpha_L^*)^{La_5Mg_{41}} > (\alpha_L^*)^{La_2Mg_{17}}$. Again a similar trend does not apply across the full temperature range considered in Fig. 3 for results from the PBEsol functional. The predicted α_L^* for La$_5$Mg$_{41}$ and La$_2$Mg$_{17}$ from PBEsol are nearly identical up to ~300 K, beyond which $(\alpha_L^*)^{LaMg_{12}} > (\alpha_L^*)^{La_5Mg_{41}} > (\alpha_L^*)^{La_2Mg_{17}}$. In general, both functionals predict that LaMg$_{12}$, the compound with the greatest x_{Mg}, has the highest α_L^* of all the La–Mg compounds.

6.4. Bulk modulus

Fig. 4 compares the isothermal $B(T)$ computed from the PBE and the PBEsol functionals for Mg and La. Experimental data for Mg from Rao [112] shows favorable agreement with the PBEsol result up to 300 K. No experimental $B(T)$ data could be located for La other than the room temperature value of 24.3 GPa which is noted by the filled triangle in Fig. 4 [113]. Two values from other exchange correlation functionals are also included in Fig. 4 (filled square LDA, and filled

Table 3
Lattice constants *a*, *c* (in Å) of the La–Mg compounds at 0 K and 298 K, from the QHA with the PBE and PBEsol functionals. Numbers in parentheses are the VASP-optimized lattice constants based upon electronic energies. Experimental results are assumed at 298 K.

	LaMg		LaMg$_2$		LaMg$_3$		La$_5$Mg$_{41}$		La$_2$Mg$_{17}$		LaMg$_{12}$	
PBE												
Å	0 K	298 K	0 K	298 K	0 K	298 K	0 K	298 K	0 K	298 K	0 K	298 K
a,b	3.97	3.98	8.80	8.84	7.53	7.56	14.84	14.92	10.39	10.44	10.38	10.44
	(3.95)		(8.78)		(7.50)		(14.88)		(10.36)		(10.34)	
c							10.48	10.54	10.20	10.24	5.94	5.97
							(10.44)		(10.16)		(5.92)	
PBEsol												
Å	0 K	298 K	0 K	298 K	0 K	298 K	0 K	298 K	0 K	298 K	0 K	298 K
a,b	3.91	3.92	8.70	8.73	7.45	7.47	14.73	14.79	10.31	10.36	10.30	10.36
	(3.90)		(8.68)		(7.43)		(14.68)		(10.28)		(10.27)	
c							10.40	10.45	10.12	10.17	5.90	5.93
							(10.36)		(10.09)		(5.87)	
a,b	3.97[a]		8.806[b]		7.51[b]		14.822[c]		10.36[d], 10.35[e]		10.33[f]	
c							10.468[c]		10.24[d], 10.25[e]		5.96[f]	

[a] Ref. [49].
[b] Ref. [52].
[c] Ref. [27].
[d] Ref. [59].
[e] Ref. [108].
[f] Ref. [65] lattice constants of CeMg$_{12}$ (ThMn$_{12}$) which is a reference structure for LaMg$_{12}$.
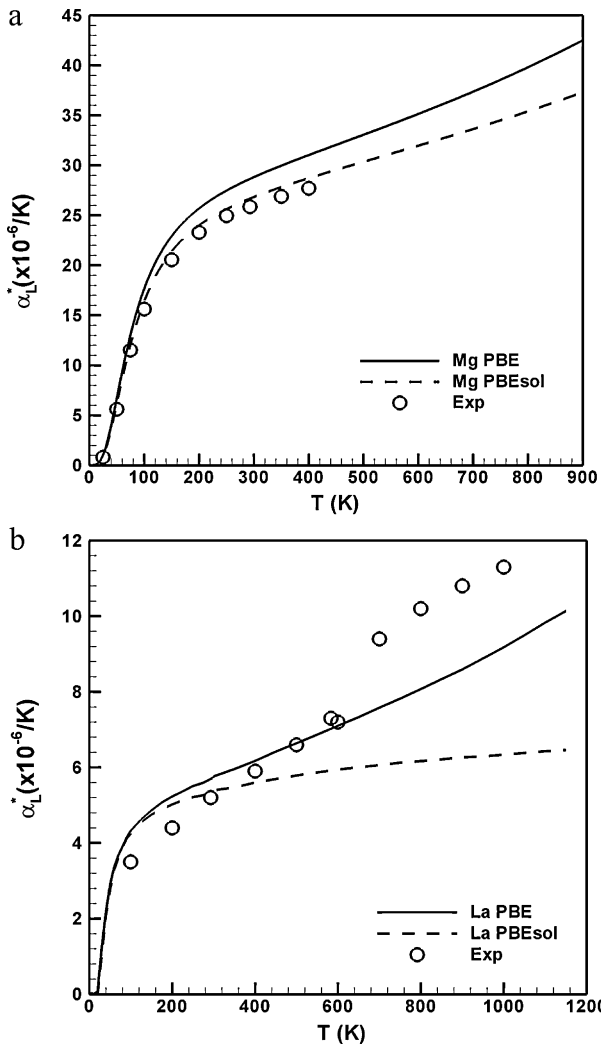
Fig. 1. Temperature (K) variation of α_L^* ($\times 10^{-6}$/K) for (a) hcp Mg, (b) dhcp La. Experimental (Exp) data for Mg and La from Refs. [109] and [110], respectively. Note that the jump in the experimental data in (b) corresponds to the dhcp α/fcc β phase transition (~600 K) in La which is not accounted for in the calculations.
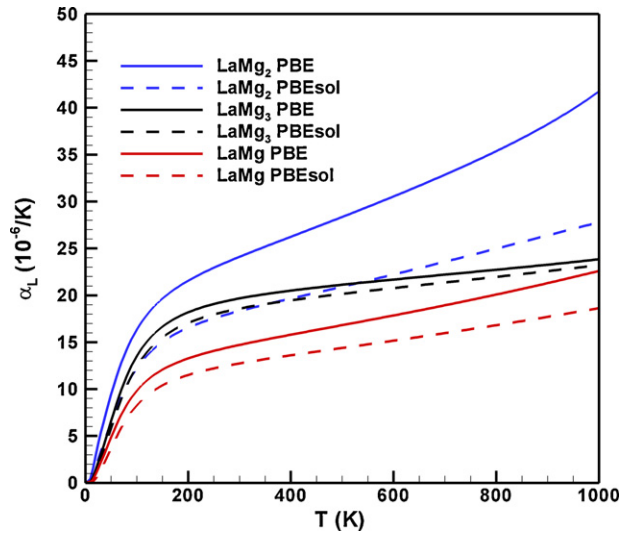

Fig. 2. Temperature (K) variation of α_L ($\times 10^{-6}$/K) for the cubic La–Mg compounds from the PBE and the PBEsol functionals.
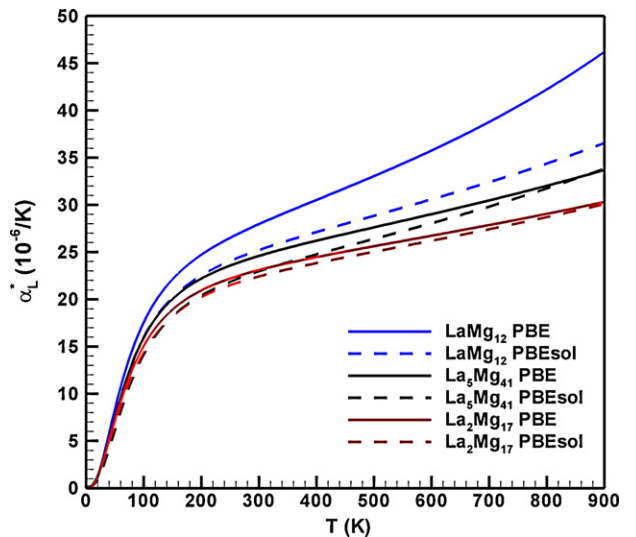

Fig. 3. Temperature (K) variation of α_L^* ($\times 10^{-6}$/K) for the non-cubic La–Mg compounds from the PBE and the PBEsol functionals.
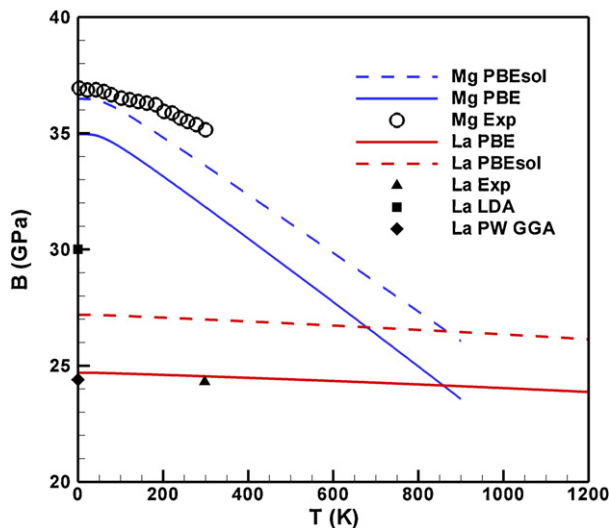
Fig. 4. Comparison of B (GPa) vs. T (K) from the PBE and the PBEsol functionals for Mg and La. Experimental data for Mg and La from Refs. [112] and [113], respectively. Additional theoretical values for La taken from Ref. [114]. Note: PW = Perdew-Wang [115].

triangle GGA). For much of the temperature range considered in Fig. 4, the $B(T)$ for Mg exceeds that of La.

Fig. 5 compares the $B(T)$ for the cubic La–Mg compounds computed with the PBE and the PBEsol. For both functionals, LaMg$_3$ (with the largest x_{Mg} of the cubic materials) is predicted to have the greatest $B(T)$, while $B(T)_{LaMg_2} > B(T)_{LaMg}$ at lower T. This trend reverses at higher T ($\sim$325 K).

Fig. 6 shows the $B(T)$ for the non-cubic La–Mg compounds computed with the PBE and the PBEsol. The PBE predicts the $B(T)$ for LaMg$_{12}$ to be smaller than the $B(T)$ computed for La$_5$Mg$_{41}$ and La$_2$Mg$_{17}$. Minimal differences are noted between La$_5$Mg$_{41}$ and La$_2$Mg$_{12}$ from the PBEsol for the range of T considered in the figure, while a larger variation is suggested by the PBE.

6.5. Heat capacity

Fig. 7a and b show the C_p (T) from the QHA for Mg and La, respectively, compared with experiment [116]. We note that both the PBE
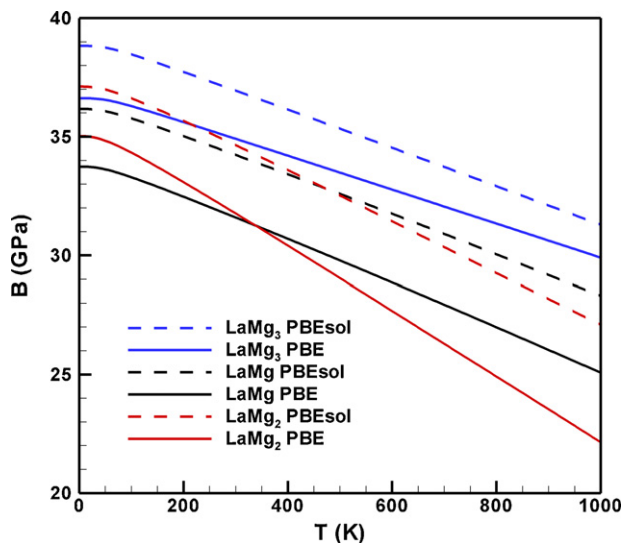

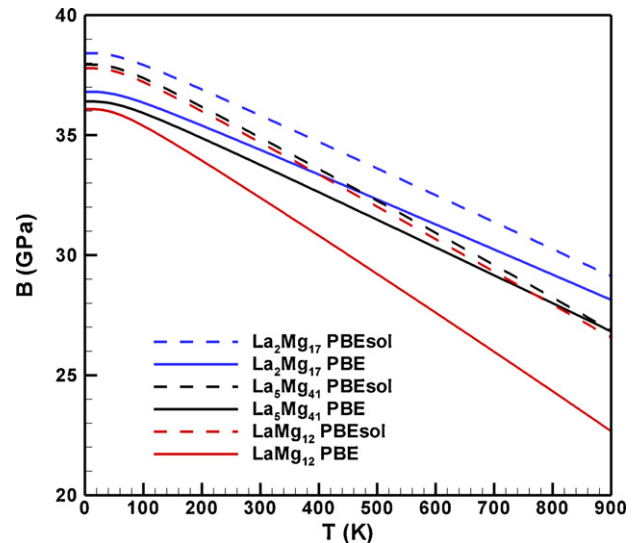**Fig. 6.** Comparison of B (GPa) vs. T (K) from the PBE and the PBEsol functionals for La$_5$Mg$_{41}$, La$_2$Mg$_{17}$, LaMg$_{12}$.

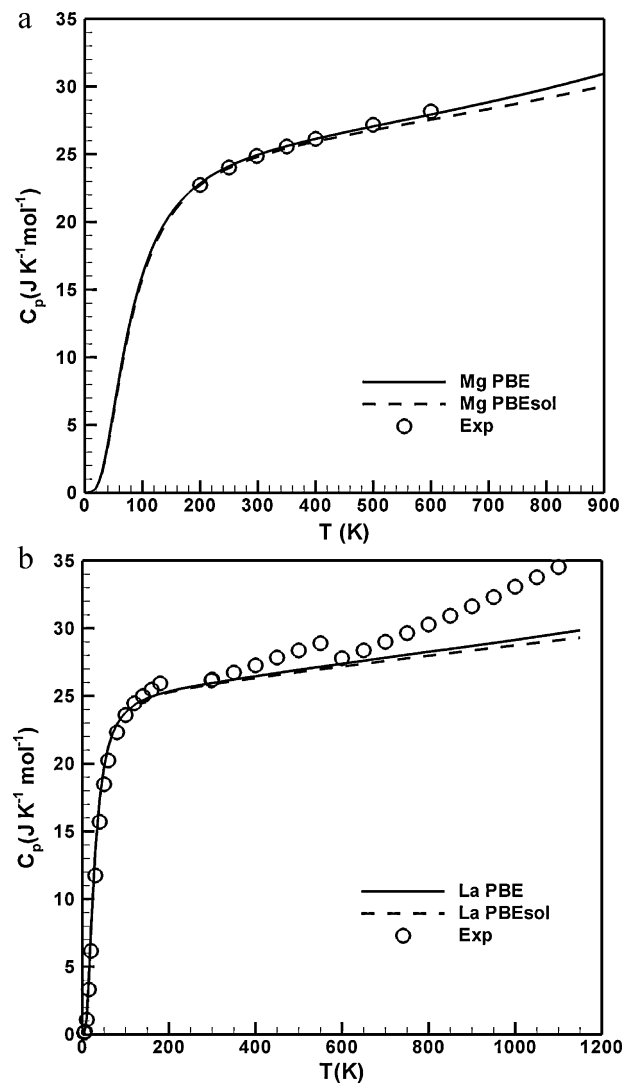**Fig. 5.** Comparison of B (GPa) vs. T (K) from the PBE and the PBEsol functionals for LaMg, LaMg$_2$, and LaMg$_3$.

Fig. 7. Temperature (K) variation of C_p (J K^{-1} mol^{-1}) from the PBE and the PBEsol functionals for (a) hcp Mg, (b) dhcp La. Experimental (Exp) data for Mg and La from Ref. [116]. Note that the jump in the experimental data in (b) corresponds to the dhcp/fcc phase transition ($\sim$600 K) in La which is not addressed in the calculations.
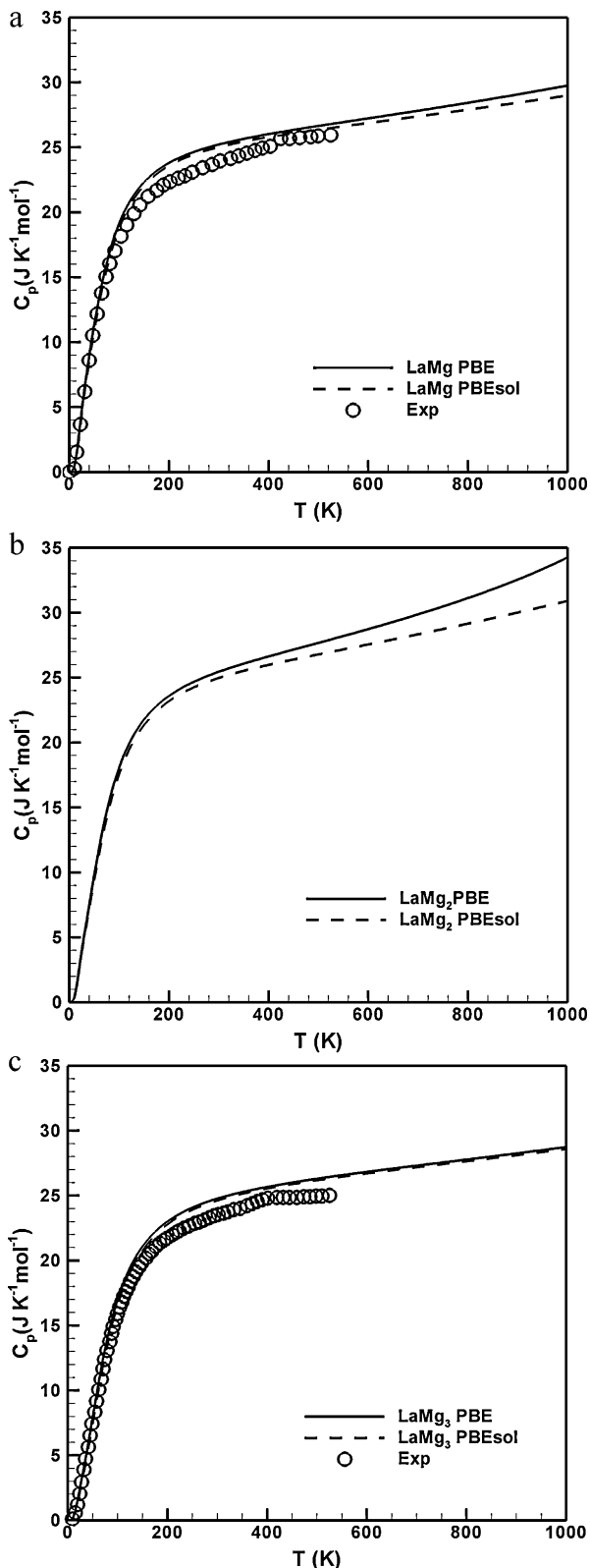
Fig. 9. Comparison on C_p (J K^{-1} mol^{-1}) vs. T (K) from the PBE and the PBEsol functionals for La$_5$Mg$_{41}$, La$_2$Mg$_{17}$, LaMg$_{12}$..

Fig. 8. Comparison on C_p (J K^{-1} mol^{-1}) vs. T (K) from the PBE and the PBEsol functionals for (a) LaMg, (b) LaMg$_2$, (c) LaMg$_3$. Experimental data in (a) and (c) from Refs. [51] and [56], respectively.
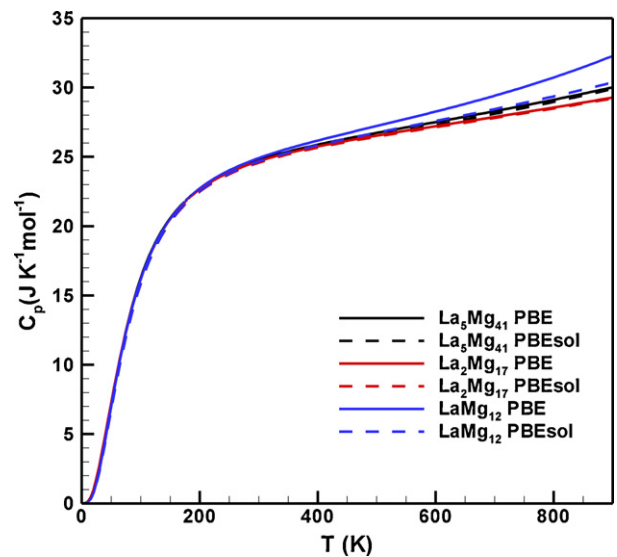
and the PBEsol yield good agreement with experimental data for Mg. As expected, the experimental $C_p(T)$ data for La shows a jump at ~600 K corresponding to the dhcp α/fcc β phase transition. Again, this is not captured in the theoretical framework of the QHA.

Fig. 8a–c show the predicted $C_p(T)$ for the cubic La–Mg compounds. The PBEsol results are in closer accord with experimental data from the literature for LaMg [51] and LaMg$_3$ [56]. However, all three figures suggest only very minimal differences between the PBE and the PBEsol.

Fig. 9 compares the predicted $C_p(T)$ for the non-cubic La–Mg compounds. Deviations between the three materials are most notable at higher temperature (~T > 400 K) with the $C_p(T)$ for LaMg$_{12}$ exceeding that for La$_5$Mg$_{41}$ and La$_2$Mg$_{17}$.

6.6. Enthalpy of formation and phase stability

Table 4 lists the computed enthalpies of formation for each La–Mg compound with the reference states being dhcp La and hcp Mg. Note that ΔH_0 and ΔH_{298} are the enthalpies of formation corresponding to 0 K (including zero point energy), and 298 K, respectively. Also listed in Table 4 are enthalpies of formation from other calculations (ΔH_{calc}) and experiments (ΔH_{exp}) as well as stability ranges for all materials considered. Results from other calculations, for which other GGA functionals are used and no zero point and finite temperature effects are included, tend to be closer to the ΔH_{static} from the PBE in the present study with the single exception being LaMg$_{12}$. The spread of previously calculated formation enthalpies as well as those obtained here from PBE and PBEsol is much smaller than the spread between available experimental data [25,118,119]. Results from the PBE for ΔH_{298} tend to be closer to the experimental values of Refs. [25] and [118] (only for LaMg$_{12}$ is PBEsol closer), whereas experimental data of Ref. [119] deviate considerably from computed and other experimental data.

In general, the computed enthalpies of formation at 0 K and 298 K in Table 4 suggest greater thermodynamic stability from the PBE than that from PBEsol for the La–Mg compounds, but no conclusions can be drawn without a phase stability analysis. Fig. 10 investigates phase stability of the La–Mg compounds from PBE- and PBEsol-computed enthalpies of formation based upon VASP electronic energies. Two compounds in particular, i.e. LaMg$_2$ and La$_5$Mg$_{41}$, do not lie on the convex hull shown in Fig. 10a. This is true

Table 4
Enthalpies of formation ΔH_0 and ΔH_{298} at 0 K and 298 K, respectively, calculated in the PBE (PBEsol) compared with other theoretical calculations (ΔH_{calc}) and experimental values (ΔH_{exp}). All results are in kJ/mol/atom to facilitate comparisons with experimental data. T_{range} = range of stability (K).

	LaMg	LaMg$_2$	LaMg$_3$	La$_5$Mg$_{41}$	La$_2$Mg$_{17}$	LaMg$_{12}$
ΔH_0	−10.85	−11.66	−12.65	−7.27	−7.33	−5.56
	(−8.69)	(−10.09)	(−12.28)	(−8.42)	(−6.26)	(−4.80)
ΔH_{298}	−10.95	−11.75	−12.80	−7.34	−7.43	−5.63
	(−8.89)	(−10.20)	(−12.47)	(−8.51)	(−6.35)	(−4.88)
ΔH_{calc}	−11.3[a]	−12.2[a]	−13.3[a]		−7.7[a]	
	−13.1[b]	−12.0[b]	−9.0[b]		−4.1[b]	
	−13.0[c]		−9.6[c]		−4.1[c]	−3.0[c]
	−11.3[d]		−17.3[d]		−7.8[d]	
ΔH_{exp}	−11.9[e]		−13.5[e]			
	−7.1[f]	−2.4[f]	−27.7[f]		−0.7[f]	
	−12.1 ± 3.4[g]	−15.8 ± 3.5[g]	−15.7 ± 2.4[g]		−7.8 ± 1.7[g]	−4.9 ± 1.7[g]
T_{range}	<1018[h,i]	899–1048[h]	<1071[h,j]	873–943[j,k]	<945[j]	<913[l]
		998–1053[i]				

[a] Ref. [32] VASP, GGA, 0K, zero point contribution not included.
[b] Ref. [117].
[c] Ref. [24] Miedema model.
[d] Ref. [118] QUANTUM-ESPRESSO PWscf ab-initio package, GGA, Vanderbilt ultrasoft pseudopotentials.
[e] Ref. [25] Acid calorimetry (in hydrochloric acid) at 298 K.
[f] Ref. [119] Acid calorimetry (in hydrochloric acid) at 298 K.
[g] Ref. [118] metallic calorimetry at 298K (a custom Tian-Calvet calorimeter).
[h] Ref. [23].
[i] Ref. [120].
[j] Ref. [28].
[k] Ref. [48].
[l] Ref. [121].

for both PBE and PBEsol, and details are shown in Fig. 10b for LaMg$_2$ and Fig. 10c for La$_5$Mg$_{41}$. Since no imaginary phonon modes have been computed in any of the vibrational spectra (see supplementary material), both compounds are predicted to be metastable at low temperatures. Our results are in agreement with those of Zhang

et al. [30] who previously predicted low temperature metastability of LaMg$_2$. However, the La$_5$Mg$_{41}$ compound was not investigated in their study.

We may estimate the temperatures at which LaMg$_2$ and La$_5$Mg$_{41}$ become stable by finding the temperature at which the

Table 5
Calculated PBE (PBEsol) C_{ij} and bulk (B), shear (G) and Young's (E) moduli based upon VASP electronic energies (i.e. no QHA). Polycrystalline bulk (B), shear (G), and Young's (E) moduli are derived from the Hill criterion. All moduli are in GPa.

	Mg	La	LaMg	LaMg$_2$	LaMg$_3$	La$_5$Mg$_{41}$	La$_2$Mg$_{17}$	LaMg$_{12}$
C_{11}	60.3	50.2	47.4	58.0	59.3	71.7	74.7	87.1
	(60.4)	(57.7)	(48.6)	(61.7)	(63.2)	(77.6)	(77.4)	(91.4)
C_{12}	28.8	14.8	28.7	25.0	26.5	16.9	21.9	10.2
	(31.4)	(16.7)	(30.7)	(26.0)	(27.9)	(19.6)	(23.8)	(13.1)
C_{13}	21.7	10.2	–	–	–	17.5	16.3	17.8
	(22.0)	(8.4)				(19.4)	(16.6)	(15.6)
C_{33}	66.6	51.8	–	–	–	74.8	81.3	72.1
	(68.4)	(62.1)				(80.5)	(85.7)	(81.2)
C_{44}	15.7	15.1	36.9	22.2	36.6	28.8	25.6	26.5
	(15.1)	(17.7)	(39.7)	(18.9)	(39.5)	(31.7)	(28.2)	(28.1)
C_{66}	–	–	–	–	–	17.7	–	23.2
						(18.6)		(23.3)
B	36.8	24.7	34.9	36.0	37.4	35.8	37.7	37.5
	(37.8)	(27.1)	(36.7)	(37.9)	(39.7)	(39.2)	(39.5)	(39.1)
G	16.9	17.2	21.4	19.8	26.5	25.7	27.2	28.2
	(16.3)	(20.5)	(22.1)	(18.5)	(28.6)	(27.6)	(28.8)	(30.1)
E	44.0	41.9	53.0	49.9	64.3	62.1	65.7	67.6
	(42.7)	(49.9)	(54.7)	(47.7)	(69.1)	(67.0)	(69.6)	(71.8)
Experimental and other theoretical data								
C_{11}	63.5[a], 58.1[b], 67.5[c]	51.4[c]	46.7[e], 44.7[f]	58.4[e]	59.2[e], 59.1[g]			
C_{12}	25.9[a], 27.6[b], 24.8[c]	17.3[c]	27.8[e], 29.4[f]	24.9[e]	26.2[e], 26.3[g]			
C_{13}	21.7[a], 21.6[b], 24.1[c]	10.4[c]						
C_{33}	66.5[a], 64.7[b], 72.4[c]	54.6[c]						
C_{44}	18.4[a], 14.2[b], 24.0[c]	13.9[c]	36.2[e], 35.1[f]	21.8[e]	36.0[e], 35.9[g]			
B	36.9[a], 39.2[c], 35.5[d]	25.9[c], 24.3[d]	34.1[e], 34.5[f]	36.0[e]	37.2[e], 37.2[g]			
G	19.3[a], 22.8[c], 17.4[d]	16.7[c], 14.9[d]	25.5[e], 19.5[f]	19.7[e]	28.2[e], 26.3[g]			
E	43.5[a], 57.3[c], 44.4[d]	41.2[c], 38.0[d]	61.2[e], 49.3[f]	50.1[e]	67.5[e], 63.9[g]			

[a] Ref. [108] experimental data.
[b] Ref. [122] VASP/PAW/GGA-PW91 and the strain vs. stress method.
[c] Ref. [123] VASP/PAW/GGA-PW91 and the strain vs. strain energy method.
[d] Ref. [124] experimental data.
[e] Ref. [40] Ab-initio, GGA.
[f] Ref. [33] Ab-initio, GGA PW91.
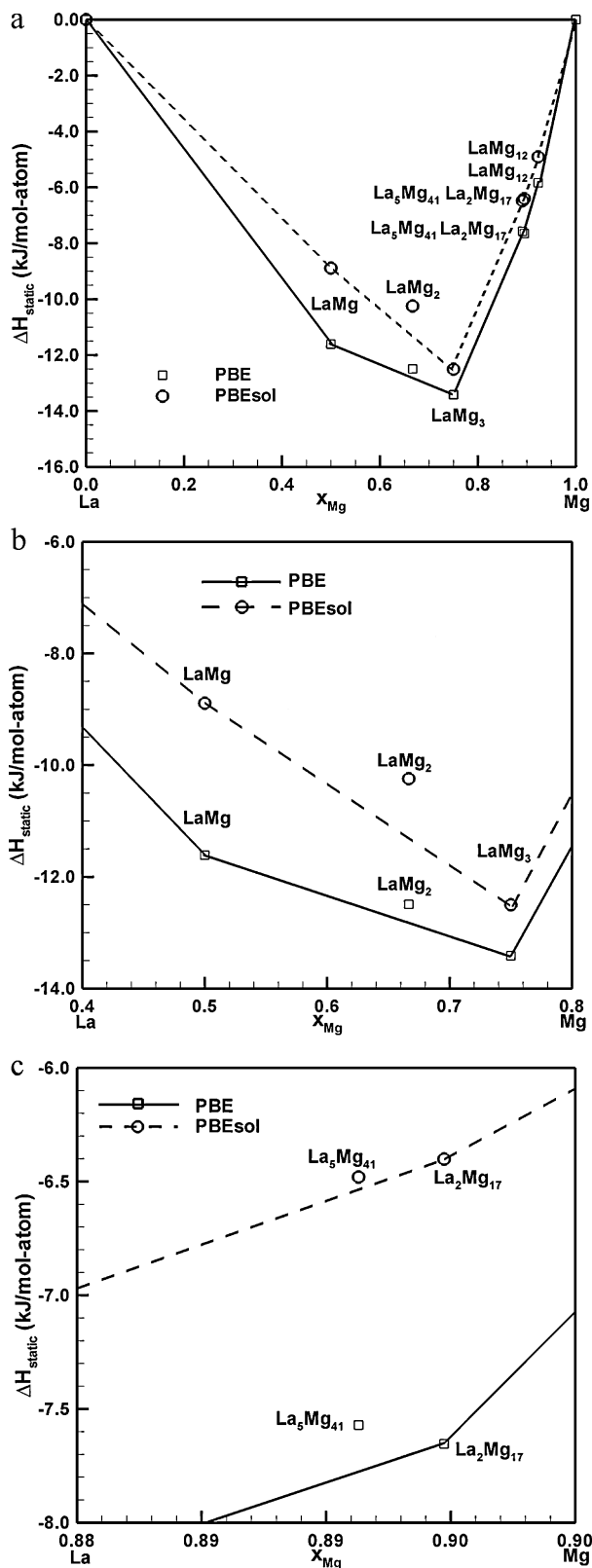[g] Ref. [29] Ab-initio, GGA PW91.

Fig. 10. First-principles calculated enthalpies of formation at 0 K for La–Mg compounds (a) together with the zoomed in parts around $LaMg_2$ (b) and La_5Mg_{41} (c). Clearly $LaMg_2$ and La_5Mg_{41} are inside the convex hull, indicating they are not stable at low temperatures with respect to their neighbors. We therefore define them as metastable phases in the present study.
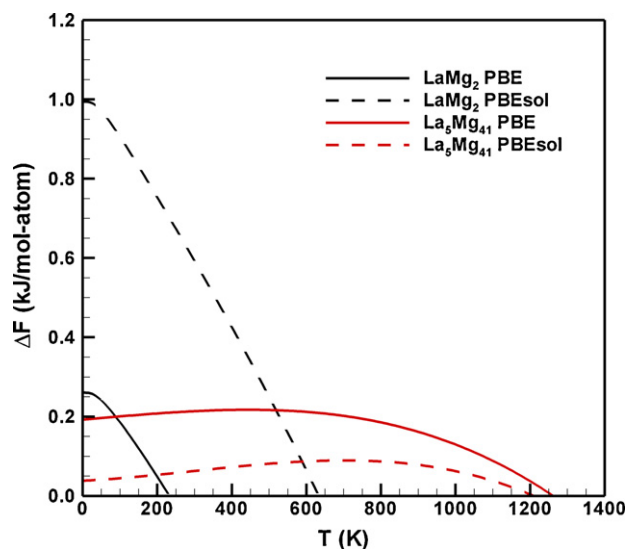

Fig. 11. Variation of relative Helmholtz free energy, ΔF, with T (K) for $LaMg_2$ and La_5Mg_{41}. Stability is predicted at those temperatures for which $\Delta F = 0$.

relative Helmholtz free energy, ΔF, is zero for both compounds, where $LaMg_2$ is with respect to a mixture of $LaMg$ and $LaMg_3$, and La_5Mg_{41} is with respect to a mixture of $LaMg_3$ and La_2Mg_{17}. This is accomplished in Fig. 11. Based upon the PBE, both $LaMg_2$ and La_5Mg_{41} are stable at temperatures above 223 K and 1285 K, respectively. From the PBEsol, both $LaMg_2$ and La_5Mg_{41} become stable at temperatures above 634 K and 1200 K, respectively. The phase diagram of Berche et al. [28] indicates that both phases become stable ~900 K., suggesting that the PBEsol results are in closer accord with experiments. Omitted in our analysis is the effect of $LaMg_3$ composition [28]: this may introduce error in our estimates of $LaMg_2$ and La_5Mg_{41} phase stability. Despite this, we believe that DFT provides the correct trends.

6.7. Elasticity tensor components

Table 5 lists the computed elasticity tensor components, C_{ij}, for the La–Mg compounds from PBE (PBEsol values are in parentheses) at 0 K without the effect of the zero point energy. The polycrystalline bulk (B), shear (G), and Young's (E) moduli are derived from the computed C_{ij} using the Hill criterion detailed in Hector et al. [97]. Results from experiments and other ab initio calculations are also listed in Table 5. The C_{ij} from the PBEsol are generally larger than those from the PBE, as expected, due to the smaller computed lattice constants (see Table 3). There are, however, some exceptions. For example, the C_{44} for Mg and $LaMg_2$ and C_{13} for $LaMg_{12}$ from PBEsol are actually smaller than corresponding PBE results. Previous results for the Mg C_{44} from PW91 and LDA were 14.2 and 16.1 GPa, respectively [82]. The PBE results for the cubic La–Mg C_{ij} from VASP electronic energies are in closer accord with the literature values than are values from the PBEsol because most studies were performed with functional behaving like PBE. No experimental C_{ij} data could be located for the La–Mg compounds. Note that La_2Mg_{17} has the highest B and G polycrystalline moduli of all the La-Mg compounds considered in Table 5, while $LaMg_{12}$ has the highest Young's modulus, E. The polycrystalline B for the La–Mg compounds are close to that for Mg, while the G and E values tend to exceed those of Mg.

The independent isothermal (C_{ij}^T) and isentropic (C_{ij}^S) elasticity tensor components computed from Eqs. (6) and (7) within the

Table 6
Independent isothermal (C_{ij}^T) and isentropic (C_{ij}^S) elasticity tensor components at $T = 0, 300, 600\,\text{K}$). C_{ij} at $T = 0\,\text{K}$ account for the zero-point energy. All moduli in GPa.

Materials	T	Method	C_{11}	C_{12}	C_{13}	C_{33}	C_{44}	C_{66}
Mg	0		57.2	26.9	20.5	62.6	14.9	–
			(60.3)	(28.8)	(21.7)	(66.6)	(15.7)	
		Exp[a]	63.5	25.9	21.7	66.5	18.4	–
		Calc[b]	58.1	27.6	21.6	64.7	14.2	–
		Calc[c]	67.5	24.8	24.1	72.4	24.0	
	300	C_{ij}^T	53.6	24.6	19.0	58.3	14.0	–
		C_{ij}^S	55.0	26.0	20.3	59.6	14.0	–
		Exp[a]	59.4	25.6	21.4	61.6	16.4	–
	600	C_{ij}^T	47.8	21.0	16.6	51.4	12.7	–
		C_{ij}^S	51.0	24.1	19.7	54.5	12.7	–
La	0		49.2	14.8	10.4	51.3	14.9	–
			(50.2)	(14.8)	(10.2)	(51.9)	(15.1)	
		Calc[c]	51.4	17.3	10.4	54.6	13.9	–
	300	C_{ij}^T	48.1	14.5	10.2	50.1	14.6	–
		C_{ij}^S	48.3	14.7	10.4	50.3	14.6	–
	600	C_{ij}^T	46.8	14.2	10.0	48.8	14.4	–
		C_{ij}^S	47.1	14.6	10.3	49.1	14.4	–
LaMg	0		46.2	27.7	–	–	36.2	–
			(47.4)	(28.7)			(36.9)	
	300	C_{ij}^T	45.0	26.6	–	–	35.4	–
		C_{ij}^S	45.4	27.1	–	–	35.4	–
	600	C_{ij}^T	43.0	25.0	–	–	34.2	–
		C_{ij}^S	44.2	26.2	–	–	34.2	–
LaMg$_2$	0		46.2	27.7	–	–	36.2	–
			(58.0)	(25.0)			(22.2)	
	300	C_{ij}^T	56.7	24.4	–	–	22.0	–
		C_{ij}^S	54.0	23.0	–	–	21.8	–
	600	C_{ij}^T	54.9	23.9	–	–	21.8	–
		C_{ij}^S	50.3	21.1	–	–	21.4	–
LaMg$_3$	0		57.6	25.6	–	–	34.8	–
			(59.3)	(26.5)			(36.6)	
	300	C_{ij}^T	55.0	24.2	–	–	33.5	–
		C_{ij}^S	55.9	25.0	–	–	33.5	–
	600	C_{ij}^T	51.3	22.2	–	–	31.7	–
		C_{ij}^S	53.0	23.9	–	–	31.7	–
La$_5$Mg$_{41}$	0		71.4	18.1	17.5	74.9	30.0	19.1
			(71.7)	(16.9)	(17.5)	(74.8)	(28.8)	(17.7)
	300	C_{ij}^T	67.6	16.8	16.0	71.3	28.9	18.6
		C_{ij}^S	68.8	18.0	17.2	72.5	28.9	18.6
	600	C_{ij}^T	61.9	14.8	13.8	65.8	27.1	17.8
		C_{ij}^S	64.6	17.4	16.5	68.4	27.1	17.8
La$_2$Mg$_{17}$	0		73.0	21.4	15.1	80.6	26.7	–
			(74.7)	(21.9)	(16.3)	(81.3)	(25.6)	
	300	C_{ij}^T	69.7	19.8	13.7	76.8	25.8	–
		C_{ij}^S	70.8	20.9	14.8	78.0	25.8	–
	600	C_{ij}^T	64.5	17.4	11.6	71.1	24.4	–
		C_{ij}^S	66.9	19.8	14.0	73.5	24.4	–
LaMg$_{12}$	0		84.3	9.4	17.8	67.9	26.4	23.1
			(87.1)	(10.2)	(17.8)	(72.1)	(26.5)	(23.2)
	300	C_{ij}^T	79.7	8.0	16.2	63.6	25.5	22.2
		C_{ij}^S	81.2	9.5	17.7	65.1	25.5	22.2
	600	C_{ij}^T	72.2	5.9	13.7	56.7	24.0	20.7
		C_{ij}^S	75.9	9.6	17.5	60.5	24.0	20.7

[a] Ref. [108] experimental data.
[b] Ref. [122] VASP/PAW/GGA-PW91 and the strain vs. stress method.
[c] Ref. [123] VASP/PAW/GGA-PW91 and the strain vs. strain energy method.

QHA are listed at 0, 300, and 600 K in Table 6 (PBE only) for all materials considered in this study. Parenthetical values are the PBE predictions based upon VASP electronic energies and are taken from Table 5. In general, the C_{ij}^T and the C_{ij}^S decrease with increasing T. In addition, the C_{ij}^S, which account for the faster speed of elastic waves relative to heat diffusion, are equal to or greater than their isothermal counterparts, C_{ij}^T, at the 300 and 600 K investigated herein. The notable exception is LaMg$_2$.

6.8. Elastic anisotropy

Crystalline materials very rarely can be characterized by a single value of the Young's modulus as its value depends on the direction within a crystal lattice in which it is measured. A convenient representation of anisotropy is a plot of a Young's modulus surface. Fig. 12 shows Young's modulus surfaces for each of the six La–Mg compounds computed with the procedure outlined
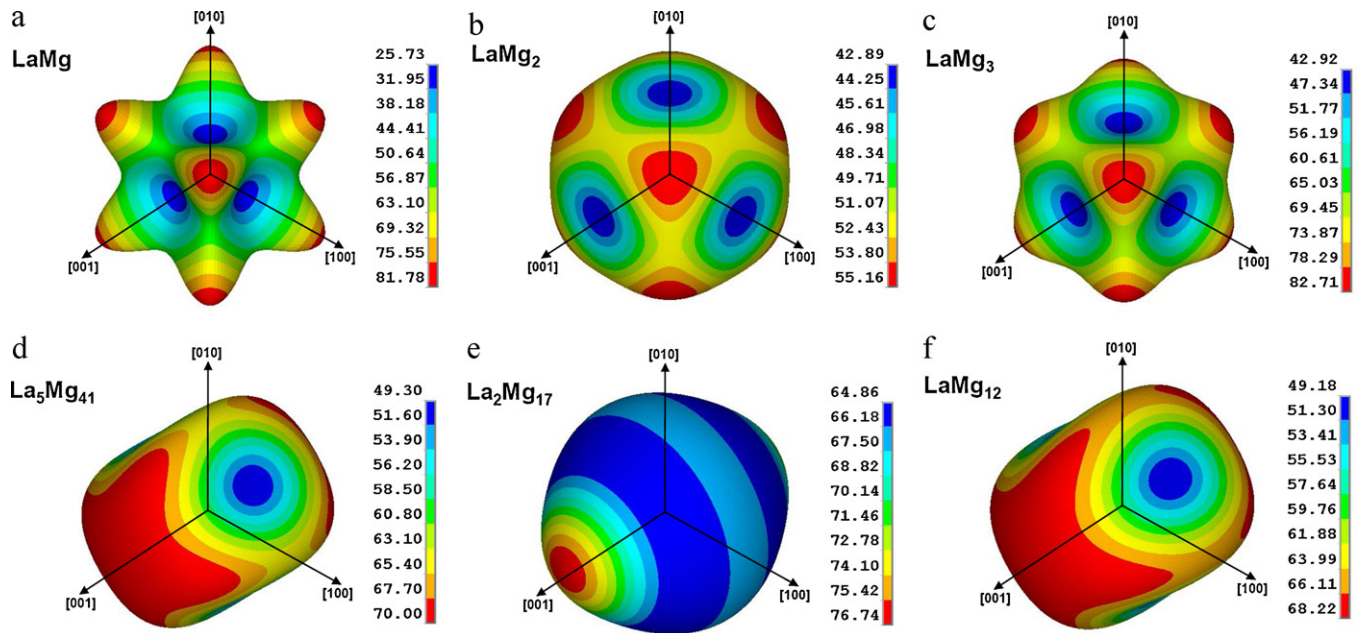
Fig. 12. Young's modulus (GPa) surfaces for (a) LaMg, (b) LaMg$_2$, (c) LaMg$_3$, (d) La$_5$Mg$_{41}$, (e) La$_2$Mg$_{17}$, (f) LaMg$_{12}$.

in Section 5.4. Each point on a given surface represents the magnitude of Young's modulus in the direction of a vector from the origin to a given point on the surface. In this way, the surfaces map out how the Young's modulus varies with crystallographic direction. When the phase is elastically isotropic (or nearly so), the Young's modulus surface is spherical (or nearly so). Otherwise, the surface has a more complicated shape. For example, the surfaces for La$_5$Mg$_{41}$ and La$_2$Mg$_{17}$ in Fig. 12d,e are closer to being spherical in that they display fewer facets (or branches). Alternatively, the LaMg surface in Fig. 12a shows numerous facets and hence this material is more elastically anisotropic than either La$_5$Mg$_{41}$ or La$_2$Mg$_{17}$. The surfaces of LaMg$_2$, LaMg$_3$ and LaMg$_{12}$ in Fig. 12b,c,f fall in between these two extremes, and hence the elastic anisotropy of these materials is intermediate to that of LaMg, La$_5$Mg$_{41}$, and La$_2$Mg$_{17}$.

The variations of the Young's moduli (minimum and maximum values as well as their ratio and standard deviations) for the La–Mg intermetallic compounds associated with Fig. 12 are listed in Table 7. If it is assumed that the La–Mg compounds have randomly oriented grains, then the Young modulus can be estimated by averaging over all possible directions. The average Young's

moduli for each La–Mg phase (as included in Table 7) is higher than that for the pure Mg crystal ($E = 45$ GPa), with the highest values computed for LaMg$_3$ and La$_2$Mg$_{17}$. Additionally, La$_2$Mg$_{17}$ is the most elastically isotropic phase as it has the lowest ratio of maximum to minimum Young's moduli (E_{max}/E_{min}) and the coefficient of variation (SD/E_{av}) where SD is the standard deviation. This may be one reason why La$_2$Mg$_{17}$ strengthens the Mg$_{96}$ZnY$_2$La alloy [1]. LaMg is the most elastically anisotropic phase. Its Young's modulus along [111] is more than three times larger than that along [100].

The variations of the Poisson's ratio (minimum, maximum, average values, and standard deviations) for the La–Mg intermetallic compounds are also listed in Table 7. Fig. 13 shows the Poisson's ratio surfaces for the La–Mg compounds. Each point on the surface represents the magnitude of the Poisson ratio in the direction of a vector from the origin to a given point on the surface. Again, those materials with surfaces that are spherical (or nearly so) have lower anisotropy in their Poisson's ratios. This is quantified by ν_{max}/ν_{min} in Table 7. Hence, LaMg is predicted to have the greatest anisotropy of the Poisson's ratio while LaMg$_2$ has the least. This is indicated by the shape of the surfaces in Fig. 13a,b. The surfaces corresponding

Table 7
Selected PBE results from anisotropy analysis in Section 6.8 (based upon VASP electronic energies). Calculated minimum, maximum and average values of the Young's moduli (E_{min}, E_{max}, E_{av}) and the Poisson ratios (ν_{min}, ν_{max}, ν_{av}) as well as the standard deviations (SD) and the coefficients of variation (SD/E_{av}). All moduli and standard deviations are in GPa, the coefficient of variation is in percent (%).

	Mg	La	LaMg	LaMg$_2$	LaMg$_3$	La$_5$Mg$_{41}$	La$_2$Mg$_{17}$	LaMg$_{12}$
E_{min}	41.22	38.17	25.73	42.89	42.92	49.18	63.14	60.91
E_{max}	56.05	46.71	81.78	55.16	82.71	68.22	75.83	82.28
E_{av}	43.65	41.40	48.93	49.94	62.95	61.71	65.51	66.93
E_{max}/E_{min}	1.36	1.22	3.18	1.29	1.93	1.39	1.20	1.35
SD	2.88	1.95	14.49	3.26	10.59	5.50	2.52	5.05
SD/E_{av}	6.60	4.71	29.61	6.53	16.82	8.91	3.85	7.55
ν_{min}	0.243	0.190	0.110	0.245	0.131	0.186	0.168	0.150
ν_{max}	0.313	0.253	0.377	0.302	0.309	0.266	0.221	0.241
ν_{av}	0.302	0.232	0.266	0.269	0.219	0.213	0.211	0.202
ν_{max}/ν_{min}	1.29	1.33	3.43	1.23	2.36	1.43	1.32	1.61
SD	0.014	0.016	0.069	0.016	0.047	0.022	0.011	0.020
SD/ν_{av}	4.76	7.08	25.99	5.77	21.58	11.52	5.13	10.05
Other data								
ν			0.26[a]		0.22[b]			

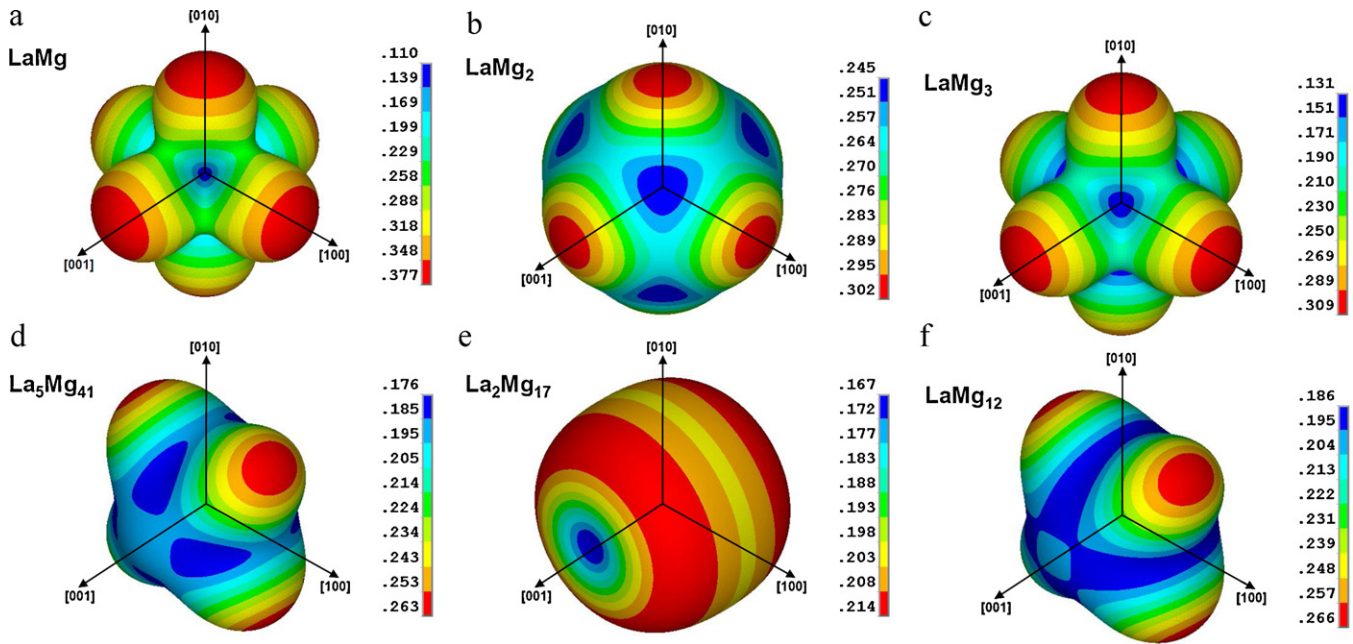[a] Ref. [33] Ab-initio, GGA PW91.
[b] Ref. [29] Ab-initio, GGA PW91.

Fig. 13. Poisson's ratio surfaces for (a) LaMg, (b) LaMg$_2$, (c) LaMg$_3$, (d) La$_5$Mg$_{41}$, (e) La$_2$Mg$_{17}$, (f) LaMg$_{12}$.

to LaMg$_3$, La$_5$Mg$_{41}$, La$_2$Mg$_{17}$, and LaMg$_{12}$ in Fig. 13c–f lie intermediate to the multi-faceted surface in Fig. 13a for LaMg, and the nearly spherical surface for LaMg$_2$ in Fig. 13b.

There is no direct link between elastic properties and plastic deformation. However, it is generally accepted that the value of the Poisson's ratio is correlated with the ductility of crystalline alloys. [125–127]. According to Cottrell's criterion [125], a small Poisson's ratio indicates lower ductility. Therefore, pure Mg with the highest averaged value of the Poisson's ratio is the most ductile material from all considered in Table 7, while La$_2$Mg$_{17}$ and La$_5$Mg$_{41}$ are possibly the least ductile.

7. Conclusions

The limited comparisons between experimental data and theoretical predictions for thermal expansion and constant pressure heat capacity suggest that results from the PBEsol are in closer accord with experiment than are the PBE results. The notable exception is La which requires special treatment of the dhcp α/fcc β phase transition. A similar observation does apply to lattice constants computed with the QHA. For the elemental metal Mg the PBEsol, and for La the PBE give lattice constants in closer accord with experiments. For the La-Mg compounds, the PBEsol-derived lattice constants for LaMg$_2$, LaMg$_3$, La$_5$Mg$_{41}$, and the lattice parameter a for La$_2$Mg$_{17}$ and LaMg$_{12}$ are closer to corresponding experimental values, whereas La-rich LaMg and the c parameters of La$_2$Mg$_{17}$ and LaMg$_{12}$ are closer within PBE (it is noted that experimental data are only available for CeMg$_{12}$).

For the cubic La–Mg compounds, the following trends are predicted:

$$\alpha_L^{LaMg_2} > \alpha_L^{LaMg_3} > \alpha_L^{LaMg} \tag{a}$$

$$\begin{cases} C_p(T)^{LaMg_2} \approx C_p(T)^{LaMg_3} \approx C_p(T)^{LaMg} \ (T \leq 400\,K) \\ C_p(T)^{LaMg_2} > C_p(T)^{LaMg_3} \approx C_p(T)^{LaMg} \ (T > 400\,K) \end{cases} \tag{b}$$

$$\begin{cases} B(T)^{LaMg_2} > B(T)^{LaMg} > B(T)^{LaMg_3} \ (T \leq 350\,K) \\ B(T)^{LaMg} > B(T)^{LaMg_2} > B(T)^{LaMg_3} \ (T > 350\,K) \end{cases} \tag{c}$$

For the non-cubic La–Mg compounds, the following trends are predicted:

$$(a_L^*)^{LaMg_{12}} > (a_L^*)^{La_5Mg_{41}} > (a_L^*)^{La_2Mg_{17}} \tag{a}$$

$$\begin{cases} C_p(T)^{LaMg_{12}} \approx C_p(T)^{La_5Mg_{41}} \approx C_p(T)^{La_2Mg_{17}} \ (T \leq 400\,K) \\ C_p(T)^{LaMg_{12}} > C_p(T)^{La_5Mg_{41}} \approx C_p(T)^{La_2Mg_{17}} \ (T > 400\,K) \end{cases} \tag{b}$$

$$B(T)^{La_2Mg_{17}} > B(T)^{La_5Mg_{41}} > B(T)^{LaMg_{12}} \tag{c}$$

The anisotropic analysis of Young's modulus and Poisson's ratio for the La–Mg compounds gives values that range from 25.73 to 82.71 GPa and 0.11–0.38, respectively. La$_2$Mg$_{17}$ is the most elastically isotropic of the 6 La–Mg compounds, while LaMg is the most elastically anisotropic.

Phase stability and vibrational spectra analyses based upon DFT suggest that LaMg$_2$ and La$_5$Mg$_{41}$ are metastable at low temperatures. From the PBE, LaMg$_2$ and La$_5$Mg$_{41}$ are thermodynamically stable at temperatures above 233 K and 1285 K, respectively. From the PBEsol, LaMg$_2$ and La$_5$Mg$_{41}$ are thermodynamically stable at temperatures above 634 K and 1200 K, respectively. Experiment suggests stability for both compounds ~900 K and hence DFT predicts the correct trends but is unable to quantitatively predict the temperatures for stability.

Appendix A. Supplementary data

Supplementary data associated with this article can be found, in the online version, at doi:10.1016/j.jallcom.2011.09.085.

References

[1] J. Rao, K. Inoue, Y. Kawamura, Adv. Eng. Mater. 7 (2005) 507–512.
[2] B. Mayer, H. Anton, E. Bott, M. Methfessel, J. Sticht, J. Harris, P.C. Schmidt, Intermetallics 11 (2003) 23–32.
[3] T.F. Smith, H.L. Luo, J. Phys. Chem. Solids 28 (1967) 569–576.
[4] X.P. Gao, Y. Wang, Z.W. Lu, W.K. Hu, F. Wu, D.Y. Song, P.W. Shen, Chem. Mater. 16 (2004) 2515–2517.
[5] L.Z. Ouyang, F.X. Qin, M. Zhu, Scripta Mater. 55 (2006) 1075–1078.
[6] H. Dong, L.Z. Ouyang, T. Sun, M. Zhu, J. Rare Earths 26 (2008) 303–306.
[7] B. Bernhardt, K. Bohmhammel, Thermochim. Acta 382 (2002) 249–254.
[8] S. Hwang, C. Nishimura, Mater. Sci. Forum 386–388 (2002) 615–620.
[9] Q.A. Zhang, Y.J. Liu, T.Z. Si, J. Alloys Compd. 417 (2006) 100–103.
[10] D.M. Liu, T.Z. Si, C.C. Wang, Q.A. Zhang, Scripta Mater. 57 (2007) 389–392.
[11] M. Khrussanova, P. Peshev, J. Mater. Sci. 23 (1988) 2247–2250.
[12] S. Yajima, H. Kayano, H. Toma, J. Less-Common Metals 55 (1977) 139–141.
[13] L. Wang, X. Wang, L. Chen, C. Chen, X. Xiao, L. Gao, Q. Wang, J. Alloys Compd. 414 (2006) 248–252.
[14] K. von Rattkay, M. Rubin, J. Appl. Phys. 85 (1999) 408–413.
[15] N.D. Saddock, A. Suzuki, J.R. TerBush, E.C. Heininger, J. Zindel, J.E. Allison, T.M. Pollock, J.W. Jones, Permanent Mold Casting and Creep Behavior of Mg–4 Al–4 X: (Ca, Ce, La, Sr) Alloys, In: A.A. Luo, N.R. Neelameggham, R.S. Beals (Eds.), Magnesium Technology 2006, TMS (The Minerals, Metals & Minerals Society), Warrendale, 2006, pp. 77–82.
[16] A. Kielbus, J. Achievements Mater. Man. Eng. 20 (2007) 459–462.
[17] Y. Fan, J. Mater. Sci. 41 (2006) 5409–5416.
[18] L. Wang, E. Guo, B. Ma, J. Rare Earths 26 (2008) 105–109.
[19] S.G. Bian, Z.Q. Li, K. Chen, J.S. Liu, J.N. Yang, Y.D. Sun, Y.L. Wang, Chin. J. Non-ferrous Metals 20 (2010) 1481–1486.
[20] G.H. Wu, H.T. Guo, X.Q. Xiao, W.J. Ding, Mater. Sci. Forum 448–489 (2005) 111–114.
[21] I.A. Anyanwu, Y. Gokan, A. Suzuki, S. Komado, Y. Kojima, S. Takeda, T. Ishida, Mater. Sci. Eng. A 380 (2004) 93–99.
[22] Z. Du, C. Guo, C. Li, W. Zhang, Rare Metals 25 (2006) 492–500.
[23] A.A. Nayeb-Hashemi, J.B. Clark, Bull. Alloy Phase Diagrams 9 (1984) 172–178.
[24] C. Guo, Z. Du, J. Alloys Compd. 385 (2004) 109–113.
[25] G. Canneri, Metall. Ital. 23 (1931) 803–823.
[26] H. Okamoto, J. Phase Equil. Diff. 27 (2006) 550, 550.
[27] M. Giovannini, A. Saccone, R. Marazza, Metall. Mater. Trans. A 26 (1995) 5–10.
[28] A. Berche, P. Benigni, J. Rogez, M.-C. Record, J. Therm. Anal. Calorim. (2011), doi:10.1007/s10973-011-1441-9.
[29] Y. Ouyang, X. Tao, Y. Feng, Y. Du, X. Zhong, Phys. Scripta 78 (2008) 065601:1–6.
[30] H. Zhang, S. Shang, J.E. Saal, A. Saengdeejing, Y. Wang, L.Q. Chen, Z.K. Liu, Intermetallics 17 (2009) 878–885.
[31] M.C. Gao, A.D. Rollett, M. Widom, Phys. Rev. B 75 (2007) 174120:1–16.
[32] Y.F. Wang, W.B. Zhang, Z.Z. Wang, Y.H. Deng, N. Yu, B.Y. Tang, X.Q. Zeng, W.J. Ding, Comp. Mater. Sci. 41 (2007) 78–85.
[33] X. Tao, Y. Ouyang, H. Liu, Y. Feng, Y. Du, Z. Jin, Solid State Commun. 148 (2008) 314–318.
[34] X. Tao, Y. Ouyang, H. Liu, F. Zeng, Y. Feng, Z. Jin, Physica B 399 (2007) 27–32.
[35] N. Saunders, A.P. Miodownik, CALPHAD (Calculation of Phase Diagrams): A Comprehensive Guide, Pergamon, Oxford/New York, 1998.
[36] Z. Du, C. Guo, W. Zhang, Rare Metals 25 (2006) 492–500.
[37] Z.K. Liu, J. Phase Equil. Diff. 30 (2009) 517–534.
[38] Z.K. Liu, JOM 60 (2008) 13–31.
[39] R. Schmid-Fetzer, J. Grobner, Adv. Eng. Mater. (2011), doi:10.1003/1527-2648(200112).
[40] S. Ganeshan, S.L. Shang, H. Zhang, Y. Wang, M. Mantina, Z.K. Liu, Intermetallics 17 (2009) 313–318.
[41] P. Villano, M. Carewska, S. Passerini, Thermochim. Acta 402 (2003) 219–224.
[42] M. Raju, J.P. Ortmann, S. Kumar, Int. J. Hydrogen Energy 35 (2010) 8742–8754.
[43] B.J. Hardy, D.L. Anton, Int. J. Hydrogen Energy 34 (2009) 2992–3004.
[44] C. Na Ranong, M. Höhne, J. Franzen, J. Hapke, G. Fieg, M. Dornheim, N. Eigen, J.M. Bellosta von Colbe, O. Metz, Chem. Eng. Technol. 32 (2009) 1154–1163.
[45] K. Onda, T. Ohshima, M. Nakayama, K. Fukuda, T. Araki, J. Power Sources 158 (2006) 535–542.
[46] A. Herman, T. Chaudhuri, P. Spagnol, Int. J. Hydrogen Energy 30 (2005) 1297–1302.
[47] H. Kim, Effects of Mechanical Stresses on Lithium Ion Batteries, University of Michigan, Ann Arbor, 2009.
[48] S. De Negri, M. Giovannini, A. Saccone, J. Alloys Compd. 427 (2007) 134–141.
[49] A. Iandelli, A. Palenzona, J. Less-Common Metals 9 (1965) 1–6.
[50] K.H.J. Buschow, J. Less-Common Metals 33 (1973) 239–244.
[51] M. Morishita, H. Yamamoto, A. Onoue, Y. Matsumoto, J. Alloys Compd. 458 (2008) 41–46.
[52] M. Giovannini, R. Marazza, A. Saccone, R. Ferro, J. Alloys Compd. 203 (1994) 155–157.
[53] B. Belgacem, S. Yahyaoui, P.Y. Demchenko, O.I. Bodak, M. Dusek, R. Ben Hassen, Acta Cryst. E61 (2005) i155–i157.
[54] V. Raghavan, J. Phase Equil. Diff. 29 (2008) 270–271.
[55] K.H.J. Buschow, J. Less-Common Metals 44 (1976) 301–306.
[56] H. Yamamoto, M. Morishita, Y. Matsumoto, A. Onoue, Mater. Trans. 48 (2007) 2159–2164.
[57] M.L. Huang, H.X. Li, H. Ding, Y.P. Ren, S.M. Hao, Acta Met. Sin. 21 (2008) 329–335.
[58] Y.B. Kang, A.D. Pelton, P. Chartrand, P. Spencer, C.D. Fuerst, J. Phase Equil. Diff. 28 (2007) 342–354.
[59] V.I. Evdokimenko, P.I. Kripyakevich, Kristallografiya 8 (1963) 135–141.
[60] Y. Chen, C.A.C. Sequeira, Mater. Sci. Forum 514-516 (2006) 452–455.
[61] L.M.C. Zarpelon, E.A. Ferreira, H. Takiishi, R.N. Faria, Mater. Sci. Forum 591-593 (2008) 879–884.
[62] M. Khrussanova, M. Terzieva, P. Peshev, Int. J. Hydrogen Energy 11 (1986) 331–334.
[63] D. Sun, F. Gingl, H. Enoki, D.K. Ross, E. Akiba, Acta Mater. 48 (2000) 2363–2372.
[64] Q. Johnson, G.S. Smith, D.H. Wood, E.M. Cramer, Nature 201 (1964) 600.
[65] D.H. Wood, E.M. Cramer, J. Less-Common Metals 9 (1965) 321–337.
[66] K. Pal, Int. J. Hydrogen Energy 22 (1997) 799–804.
[67] J. Deportes, D. Givord, R. Lemaire, H. Nagai, J. Less-Common Metals 40 (1975) 299–304.
[68] D. Sun, F. Gingl, Y. Nakamura, H. Enoki, M. Bououdina, E. Akiba, J. Alloys Compd. 333 (2002) 103–108.
[69] R.V. Denys, A.A. Poletaev, J.K. Solberg, B.P. Tarasov, V.A. Yartys, Acta Mater. 58 (2010) 2510–2519.
[70] A.A. Poletaev, R.V. Denys, J.K. Solberg, B.P. Tarasov, V.A. Yartys, J. Alloys Compd. (2010), doi:10.1016/j.jallcom.2010.09.172.
[71] G. Kresse, J. Hafner, Phys. Rev. B 49 (1994) 14251–14269.
[72] G. Kresse, J. Furthmüller, Comp. Mater. Sci. 6 (1996) 15–50.
[73] G. Kresse, J. Furthmüller, Phys. Rev. B 54 (1996) 11169–11186.
[74] P.E. Blöchl, Phys. Rev. B 50 (1994) 17953–17979.
[75] J.P. Perdew, K. Burke, M. Ernzerhof, Phys. Rev. Lett. 77 (1996) 3865–3868.
[76] J.P. Perdew, A. Ruzsinszky, G.I. Csonka, O.A. Vydrov, G.E. Scuseria, L.A. Constantin, X. Zhou, K. Burke, Phys. Rev. Lett. 100 (2008) 136406:1–4.
[77] A.E. Mattsson, R. Armiento, J. Paier, G. Kresse, J.M. Wills, T.R. Mattsson, J. Chem. Phys. 128 (2008) 084714:1–11.
[78] M. Ropo, K. Kokko, L. Vitos, Phys. Rev. B 77 195445 (2008) 195445:1–7.
[79] G.I. Csonka, J.P. Perdew, A. Ruzsinszky, P.H.T. Philipsen, S. Lebègue, J. Paier, O.A. Vydrov, J.G. Ángyán, Phys. Rev. B 79 (2009) 155107:1–14.
[80] P. Haas, F. Tran, P. Blaha, Phys. Rev. B 79 (2009) 085104:1–10.
[81] K. Parlinski, Software Phonon 4.30 as implemented in MedeA 2.5. http://www.MaterialsDesign.com; K. Parlinski, Z. Li, Y. Kawazoe, Phys. Rev. Lett. 78 (1997) 4063–4066.
[82] L.G. Hector Jr., J.F. Herbst, W. Wolf, P. Saxe, G. Kresse, Phys. Rev. B 76 (2007) 014121:1–18.
[83] Y. Duan, D.C. Sorescu, Phys. Rev. B 79 (2009) 014301:1–18.
[84] J. Xie, S. de Gironcoli, S. Baroni, M. Scheffler, Phys. Rev. B 59 (1999) 965–969.
[85] Z. Wu, R.M. Wentzcovitch, Phys. Rev. B 79 (2009) 104304:1–12.
[86] G. Grimvall, Thermophysical Properties of Matter, North-Holland, New York, 1999.
[87] T. Kelkar, D.G. Kanhere, S. Pal, Comp. Mater. Sci. 42 (2008) 510–516.
[88] Y. Wang, Z.K. Liu, L.Q. Chen, Acta Mater. 52 (2004) 2665–2671.
[89] F. Birch, Phys. Rev. 71 (1947) 809–824.
[90] R. Arroyave, D. Shin, Z.K. Liu, Acta Mater. 53 (2005) 1809–1819.
[91] J. Nye, Physical Properties of Crystals: Their Representation by Tensors and Matrices, Clarendon, Oxford, 1985.
[92] M.E. Fine, L.D. Brown, H.L. Marcus, Scripta Met. 18 (1984) 951–956.
[93] A. Baldi, M. Gonzalez-Silveira, V. Palmisano, B. Dam, R. Griessen, Phys. Rev. Lett. 102 (2009) 226102:1–4.
[94] C. Woodward, D. Trinkle, L. Hector, D. Olmsted, Phys. Rev. Lett. 100 (2008) 045507:1–4.
[95] Y. Le Page, P. Saxe, Phys. Rev. B 63 (2001) 174103:1–8.
[96] Y. Le Page, P. Saxe, Phys. Rev. B 65 (2002) 104104:1–14.
[97] L.G. Hector Jr., J.F. Herbst, T.W. Capehart, J. Alloys Compd. 353 (2003) 74–85.
[98] J.F. Lutsko, J. Appl. Phys. 65 (1989) 2991–2997.
[99] Y. Wang, J.J. Wang, H. Zhang, V.R. Manga, S.L. Shang, L.Q. Chen, Z.K. Liu, J. Phys. Cond. Matter. 22 (2010) 225404:1–8.
[100] S.L. Shang, H. Zhang, Y. Wang, Z.K. Liu, J. Phys. Cond. Matter. 22 (2010) 375403:1–8.
[101] G.F. Davies, J. Phys. Chem. Solids 35 (1974) 1513–1520.
[102] B. Yang, A.A. Volinsky, Eng. Fract. Mech. 75 (2008) 3121–3130.
[103] M. Yamamoto, T. Kitamura, T. Ogata, Eng. Fract. Mech. 75 (2008) 779–789.
[104] J.M. Zhang, Y. Zhang, K.W. Xu, V. Ji, Mater. Lett. 62 (2008) 1328–1332.
[105] J.M. Zhang, Y. Zhang, K.W. Xu, V. Ji, J. Phys. Chem. Solids 68 (2007) 503–510.
[106] G.V. Raynor, Proc. R. Soc. Lon. Ser. A 174 (1940) 457–471.
[107] B.J. Beaudry, P.E. Palmer, J. Less-Common Metals 34 (1974) 225–231.
[108] L.J. Slutsky, C. Garland, Phys. Rev. 107 (1957) 972–976.
[109] B.H. Billings, D.E. Gray, American Institute of Physics Handbook, third edn., McGraw-Hill, New York, 1972.
[110] Y.S. Touloukian, R.K. Kirby, R.E. Taylor, P.D. Desai, Thermal expansion. Metallic elements and alloys, in: Thermophysical Properties of Matter, vol. 12, Plenum, New York, 1975.

[111] K.A. Gschneidner, Rare Earth Metal Alloys, Mir, Moscow, 1965.
[112] R.R. Rao, Phys. Rev. B 10 (1974) 4173–4177.
[113] C. Kittel, Introduction to Solid State Physics, fifth edn., John Wiley & Sons, Inc, New York, 1976.
[114] L.W. Nixon, D. Papaconstantopoulos, M. Mehl, Phys. Rev. B 78 (2008) 214510:1–13.
[115] J.P. Perdew, Y. Wang, Phys. Rev. B 45 (1992) 13244–13249.
[116] Y.S. Touloukian, E.H. Buyco, Specific heat. Metallic elements and alloys, in: Thermophysical Properties of Matter, vol. 4, IFI/Plenum, New York, 1970.
[117] B. Zhang, W. Hu, X. Shu, Theory of Embedded Method and Its Application to Materials Science – Atomic Scale Materials Design Theory, Hunan University Press, Changsha, 2003.
[118] A. Berche, F. Marinelli, J. Rogez, M.C. Record, Thermochim. Acta 499 (2010) 65–70.
[119] I.N. Piagai, A.V. Vakhobov, N.G. Schmidt, O.V. Khikhareva, M.I. Numanov, Dokl. Acad. Nauk. Tadzhiskoi SSR 32 (9) (1989) 605–607.
[120] P. Manfrinetti, K.A. Gschneidner, J. Less-Common Metals 123 (1986) 267–275.
[121] B. Darriet, M. Pezat, A. Hbika, Mater. Res. Bull. 14 (1979) 377–385.
[122] S.L. Shang, A. Saengdeejing, Z.G. Mei, D.E. Kim, H. Zhang, S. Geneshan, Y. Wang, Z.K. Liu, Comp. Mater. Sci. 48 (2010) 813–826.
[123] Y.F. Ouyang, X.M. Tao, F.J. Zeng, H.M. Chen, Y. Du, Y.P. Feng, Y. He, Phys. B 404 (2009) 2299–2304.
[124] F. Seitz, D. Turnbull, Solid State Physics: Advances in Research and Applications, vol. 16, Academic Press, New York and London, 1964.
[125] A. Kelly, W. Tyson, A.H. Cottrell, Philos. Mag. 15 (1967) 567–686.
[126] S. Pugh, Philos. Mag. 45 (1954) 823–843.
[127] I.N. Frantsevich, F.F. Voronov, S.A. Bokuta, Elastic Constants and Elastic Moduli of Metals and Insulators Handbook, Naukova Dumka, Kiev, 1983.